RUFY3 links Arl8b and JIP4-Dynein complex to regulate lysosome size and positioning

Gaurav Kumar
CSIR-Institute of Microbial Technology (IMTECH)
Prateek Chawla
Indian Institute of Science Education and Research (IISER)-Mohali
Sanya Chadha
CSIR-Institute of Microbial Technology (IMTECH)
Sheetal Sharma
CSIR-Institute of Microbial Technology (IMTECH)
Kanupriya Sethi
CSIR-Institute of Microbial Technology (IMTECH)
Mahak Sharma
Indian Institute of Science Education and Research-Mohali https://orcid.org/0000-0002-4117-4790
Amit Tuli (atuli@imtech.res.in)
CSIR-Institute of Microbial Technology (IMTECH)

Article

Keywords: Lysosome, Small GTPase, Arl8b, Dynein, Microtubule

Posted Date: April 15th, 2021

DOI: https://doi.org/10.21203/rs.3.rs-345822/v1

Version of Record: A version of this preprint was published at Nature Communications on March 21st, 2022. See the published version at https://doi.org/10.1038/s41467-022-29077-y.

Abstract

The whole-cell scale spatial organization of lysosomes is regulated by their bidirectional motility on microtubule tracks. Small GTP-binding (G) protein, Arl8b, stimulates the anterograde transport of lysosomes by recruiting adaptor protein SKIP (also known as PLEKHM2), which in turn couples the microtubule motor kinesin-1. Here, we have identified an Arl8b effector, RUN and FYVE domain-containing protein family member 3, RUFY3, which drives the retrograde transport of lysosomes. Artificial targeting of RUFY3 to the surface of mitochondria was sufficient to drive their perinuclear positioning. We find that RUFY3 interacts with the JIP4-Dynein-Dynactin complex and mediates Arl8b association with the retrograde motor complex. The mobile fraction of the total lysosomes per cell was significantly enhanced upon RUFY3 depletion, suggesting that RUFY3 maintains the lysosomes clustering within the perinuclear cloud. Expectedly, RUFY3 knockdown disrupted the perinuclear positioning of lysosomes upon nutrient starvation and/or serum depletion, although lysosome continued to undergo fusion with autophagosomes. Interestingly, lysosome fission events were more frequent in RUFY3-depleted cells and accordingly, there was a striking reduction in lysosome size, an effect that was also observed in dynein and JIP4 depleted cells. These findings indicate that the dynein-dependent “perinuclear cloud” arrangement of lysosomes also regulates the size of these proteolytic compartments and, likely, their cellular roles.

Introduction

Lysosomes are heterogeneous membrane-bound organelles containing more than 60 acid hydrolases that mediate the degradation of various biological macromolecules, including proteins, carbohydrates, lipids, and nucleic acids (Ballabio and Bonifacino, 2020). Lysosomes undergo fusion with late endosomes to form the hybrid compartment known as endolysosomes. As the three compartments share many commonly analyzed membrane proteins (such as LAMP1), we collectively refer to these compartments as lysosomes. Lysosomes (LAMP1-positive population mostly) range in numbers of 50-1000 in cultured cells and are primarily present as a relatively immobile pool in the perinuclear region of the cell (sometimes referred to as the perinuclear cloud). A minor population of lysosomes escapes from the perinuclear cloud and undergoes long-range bidirectional transport on the microtubule tracks (Cabukusta and Neefjes, 2018; Jongsma et al., 2016).

Lysosomal subcellular distribution is not static and changes with the presence/absence of nutrients, growth factors, change in cytosolic pH, exposure to oxidative stress, infection etc. (Bonifacino and Neefjes, 2017; Dykes et al., 2016; Johnson et al., 2016; Korolchuk et al., 2011; Laopanupong et al., 2021; Saric et al., 2016; Takemasu et al., 2019; Tuli et al., 2013; Willett et al., 2017). More importantly, by altering lysosomal distribution, cues such as nutrients and/or growth factors influence lysosome-mediated cellular responses under these physiological conditions. For instance, depletion of nutrients and/or growth factors results in lysosome clustering in the perinuclear region, where the proteolytic compartments may have more propensity to tether and fuse with autophagosomes (Kimura et al., 2008; Korolchuk et al., 2011). The degradation of autophagic cargo and subsequent recycling of breakdown

products replenishes nutrient reserves under starvation conditions. In contrast, growth factor re-stimulation results in lysosome localization near the plasma membrane that facilitates reactivation of lysosomal-localized mTORC1 signaling complex, and consequently, gene expression required for protein synthesis (Jia and Bonifacino, 2019). Recent studies have also highlighted the role of lysosome positioning in promoting ER remodeling from sheets to tubules in the peripheral cellular space (Lu et al., 2020; Spits et al., 2021). Also, the proximity of lysosomes to focal adhesions near the plasma membrane regulates lysosome-dependent focal adhesion disassembly, and promotes growth factor-dependent activation of the mTORC1 signaling complex (Rabanal-Ruiz et al., 2021; Schiefermeier et al., 2014).

Several factors, including the continuous long-range motility on the microtubule tracks, association with the actin cytoskeleton and tethering to the ER network, regulate the spatial distribution of lysosomes at the whole-cell scale. The microtubule-based motor proteins, cytoplasmic dynein in complex with dynactin and multiple kinesin family members, promote retrograde (towards microtubule minus-end) and anterograde (towards microtubule plus-end) lysosome motility, respectively (Bonifacino and Neefjes, 2017; Hunt and Stephens, 2011). Motor proteins are recruited on the organelle membranes by association with their adaptors, generally effectors of Rab and Arf-like (Arl) small GTP-binding (G) proteins (Donaldson and Jackson, 2011; Homma et al., 2021; Kjos et al., 2018). Rab7-RILP represents a well-characterized small G protein-effector complex on lysosomes that recruits the motor dynein-dynactin complex to promote retrograde motility of lysosomes (Johansson et al., 2007; Jordens et al., 2001). Rab7 also interacts with FYCO1 to recruit kinesin-1 on lysosomes for motility towards the plasma membrane (Pankiv et al., 2010).

A key player, now well known for regulating the lysosomal spatial location, is the small G protein Arl8 (Khatter et al., 2015b). In mammalian cells, Arl8 has two paralogs, Arl8a and Arl8b, which are ~ 91% identical at the protein level and have an overlapping role in regulating lysosomal distribution. Arl8b, the better-characterized paralog, recruits its downstream effector, PLEKHM2 (also known as SKIP for SifA and Kinesin Interacting Protein) on lysosomes, which in turn recruits kinesin-1 to mediate anterograde motility of lysosomes (Hofmann and Munro, 2006; Rosa-Ferreira and Munro, 2011). Arl8 paralogs also regulate KIF1A-dependent lysosome movement to the cell periphery (Guardia et al., 2016). Arl8b-mediated lysosome positioning has been shown to regulate lysosome interaction with processes occurring near the cell periphery, including growth factor-mediated activation of mTORC1, lysosome exocytosis, lysosome-mediated ER remodeling, focal adhesion disassembly, to name a few (Jia and Bonifacino, 2019; Lu et al., 2020; Michelet et al., 2018; Pu et al., 2017; Pu et al., 2015; Schiefermeier et al., 2014). Further, the Arl8b-SKIP complex has been shown to promote tubulation of lysosomes in activated macrophages and the formation of tubular LAMP1-positive compartment (also known as *Salmonella*-induced filaments or SIFs) in *Salmonella*-infected cells (Mrakovic et al., 2012; Sindhwani et al., 2017; Tuli and Sharma, 2019). Recent work has also shown that Arl8b-mediated lysosomal transport to the cell periphery is required for the exit of β-coronaviruses from lysosomes, where the viruses reside before egress (Ghosh et al., 2020). In addition to small G proteins and their effectors, few studies have shown the role of lysosome membrane proteins complexes in recruiting the dynein-dynactin motor, for example, MCOLN1 (TRPML1)-Alg2 and TMEM55B-JIP4 complex (Li et al., 2016; Willett et al., 2017). These two starvation-induced mechanisms

mediate dynein-dependent transport and clustering of lysosomes in the perinuclear region. Recently, Septin 9 (SEPT9), one of the Septin GTP-binding proteins, has been shown to localize to lysosomes and promote dynein-dependent retrograde transport of lysosomes (Kesisova et al., 2021).

Here, we report that RUN and FYVE domain-containing protein 3 (RUFY3) binds to Arl8b and recruits the JIP4-dynein-dynactin complex on Arl8b-positive lysosomes. Using the knockout-sideways approach, we show that RUFY3 recruitment is sufficient to drive dynein-dependent perinuclear localization of mitochondria. Along with reducing the perinuclear immobile pool of lysosomes, RUFY3 silencing led to enhanced lysosome tubulation and fission, which likely explains the striking reduction of lysosomes size in these cells. A similar decrease in lysosome size was also observed in dynein and JIP4 knockdown cells. The numerous, smaller and scattered lysosomes were able to undergo fusion with incoming endocytic vesicles and degrade endocytosed EGFR and autophagic cargo. Our results show that motor and their adaptors regulate lysosome size and positioning and likely alter the degradation kinetics of lysosomal cargo.

Results

RUFY3 is an Arl8b effector that localizes to lysosomes

In the search for novel Arl8b binding partners, we performed a yeast two-hybrid assay with Arl8b as bait and human brain tissue cDNA library as prey that led to the identification of RUFY3 (NM_001037442.4; NP_001032519.1; transcript variant 1; 620 amino acids in length; longest isoform) as an interaction partner of Arl8b (**Fig. 1A**). Transcript variant 1 (hereafter referred to as RUFY3) is the longest transcript synthesized from the RUFY3 gene, which encodes for six alternatively spliced variants. Variant 2 of RUFY3 (NM_014961.5, NP_055776.1; 469 amino acids in length) is the only RUFY3 isoform that is functionally characterized and regulate polarity and axon growth in neurons and migration and invasion of cancer cells (Char and Pierre, 2020; Honda et al., 2017; Kitagishi and Matsuda, 2013; Mori et al., 2007; Wang et al., 2015; Wei et al., 2014; Xie et al., 2017).

Using yeast two-hybrid and co-immunoprecipitation approaches, we confirmed that RUFY3 interacted with the WT (wild-type) and Q75L (constitutively GTP-bound) forms of Arl8b, but not with the T34N (constitutively GDP-bound) form (**Fig. 1B-C**). Consistent with this, RUFY3 interaction with GST-tagged-Arl8b (as bait) was reduced in the presence of excess GDP as compared to GTP, suggesting that RUFY3 behaves as an effector for the small G protein (**Supplementary Fig. S1A**). We also observed the interaction of Arl8b and RUFY3 under endogenous conditions by direct immunoprecipitation of Arl8b from HEK293T cell lysates (**Fig. 1D**).

Notably, RUFY3 variant 2 did not show an interaction with Arl8b (**Supplementary Fig. S1B**). Variant 1 (620 amino acids long) and variant 2 (469 amino acids long) of RUFY3 are identical in sequence for the first 445 amino acids. The difference between the two variants lies in a stretch of residues from 446–620, present in variant 1 but not variant 2 (**Fig. 1E** and **Supplementary Fig. S1C**). Indeed, domain deletion

analysis revealed that RUFY3 mutant lacking residues 446–561 (hereafter referred to as RUFY3 (Δ446–561)), containing the FYVE-like domain) failed to bind to Arl8b (**Supplementary Fig. S1D**). More importantly, the RUFY3 fragment encompassing 441–561 residues (hereafter referred to as RUFY3 (441–561)) was sufficient for interaction with Arl8b (**Supplementary Fig. S1D**). This was corroborated using GST-pulldown assay wherein Arl8b was interacting with GST-tagged-RUFY3 (WT) and -RUFY3 (441–561) but not a deletion mutant lacking these residues (**Supplementary Fig. S1E**). To test whether the RUFY3 fragment containing 441–561 residues directly binds to Arl8b, we incubated recombinant His-Arl8b with GST or GST-tagged-RUFY3 (WT), -RUFY3 (Δ446–561) and RUFY3 (441–561). As shown in **Fig. 1F**, we found that Arl8b directly binds to the RUFY3 encompassing the 441–561 fragment.

Next, to further narrow down amino acid residues within the RUFY3 (441–561) fragment that effect binding with Arl8b, we first mutated the positively charged residues in this fragment to alanine. This selection was based on our prior study that revealed binding of effectors PLEKHM1 and SKIP to Arl8b requires arginine residues in their RUN domain (Marwaha et al., 2017). From this screening, we found that R462/K465 residues in the RUFY3 (441–561) fragment was crucial for interaction with Arl8b, as mutating these residues to alanine (RK→A) abrogated binding to Arl8b (**Fig. 1E**; **Fig. 1G-H** and **Supplementary Fig. S1F**).

We next analyzed RUFY3 localization by transfecting epitope-tagged-RUFY3 construct in HeLa cells, as none of the available anti-RUFY3 antibodies recognized the protein under endogenous conditions. We found that epitope-tagged-RUFY3 showed a cytosolic distribution primarily with few punctate structures present in the perinuclear region of the cell (see inset, **Supplementary Fig. S2A**). The presence of RUFY3-positive punctae became more prominent in cells permeabilized with detergent before fixation to leach out the cytosol (**Supplementary Fig. S2B**). Notably, the punctate staining of RUFY3 was strongly confined to the perinuclear region of the cell (**Supplementary Fig. S2B**). Based on our prior observation that RUFY3 interacts with the lysosomal small G protein Arl8b, we chose to co-stain these cells with the late endosomal/lysosomal (LE/Lys) markers. Indeed, several RUFY3 punctae were colocalized with LAMP1 and CD63 in the perinuclear region (see yellow arrowheads in the inset, **Supplementary Fig. S2B-C**; quantification is shown in **Supplementary Fig. S2F-G**). To better resolve RUFY3 and LAMP1 colocalized structures, we used structured illumination microscopy (SIM) that showed RUFY3 was present on a specific site on the LAMP1 vesicle or closely associated with the LAMP1 (see inset, **Fig. 1I**). We also noted that few RUFY3 punctae were negative for the lysosomal markers (see white arrowheads in the inset, **Supplementary Fig. S2B-C**). Next, we analyzed whether RUFY3 also localizes to other endosomal compartments. However, no significant overlap of RUFY3 with early (Early Endosome Antigen 1-EEA1) and recycling endosome markers (Transferrin Receptor-TfR) was observed (see inset, **Supplementary Fig. S2D-E**; quantification is shown in **Supplementary Fig. S2F-G**), suggesting that RUFY3 is primarily associated with lysosomes in the endolysosomal pathway.

To further corroborate whether RUFY3 localizes to lysosomes under endogenous conditions, we used the recently described LYSO-IP method that relies on immuno-purification of subcellular compartments containing the lysosomal transmembrane protein TMEM192 (Abu-Remaileh et al., 2017). We confirmed

that the lysosomal fractions obtained using the LYSO-IP method was not contaminated with other membranes by probing for various organelle markers (**Fig. 1J**). RUFY3, similar to LAMP1 and Arl8b, was present in the lysosomal fractions under endogenous conditions, confirming the localization observed with the RUFY3-tagged construct (**Fig. 1J**). Since small G proteins are known to recruit their effectors to target membranes, we analyzed whether Arl8b plays a similar role and recruits RUFY3 on lysosomes. Indeed, RUFY3 lysosomal localization was enhanced by co-expression with Arl8b, whereas depletion of Arl8b significantly reduced RUFY3 recruitment to lysosomes (see inset, **Fig. 1K-M**; quantification is shown in **Fig. 1N-O**). Enhanced recruitment of RUFY3 on individual LAMP1-positive vesicles was also clearly evident in SIM images (see inset, **Fig. 1P**). We found that several RUFY3 punctae were still present in Arl8b siRNA-treated cells, but these were no longer colocalized with LAMP1 (see inset, **Fig. 1M**). It is unclear whether these RUFY3 punctae in Arl8b-depleted cells represent protein aggregates or some membrane-bound compartment.

RUFY3 promotes the perinuclear positioning of lysosomes

Interestingly, we found that upon RUFY3 transfection in cells, lysosomes appeared to be strongly clustered in the perinuclear region (compare untransfected and transfected cells in **Fig. 2A**). To corroborate this observation, we quantified the cumulative integrated LAMP1 intensity in cells transfected with either vector control or different RUFY3 constructs (**Fig. 2D-E**). As shown in **Fig. 2D**, the distribution of lysosomes in RUFY3 (WT) transfected cells was significantly shifted to the perinuclear region (0–5 μm) and away from the peripheral region (> 15 μm). Importantly, RUFY3 mutant proteins defective in binding to Arl8b (i.e. RUFY3 (Δ446–561) and RUFY3 (RK→A)) did not localize to the LAMP1 compartment or alter lysosome positioning, suggesting that association with Arl8b is required for RUFY3 lysosomal localization (**Fig. 2B-C**; quantification is shown in **Fig. 2D**).

From several previous studies, it is known that Arl8b is enriched on peripheral lysosomes, and its overexpression drives lysosomes accumulation near the plasma membrane (see inset, **Fig. 2F**) (Garg et al., 2011; Hofmann and Munro, 2006; Khatter et al., 2015a; Khatter et al., 2015b). This is attributed to Arl8b interaction with a RUN domain-containing protein, SKIP that binds and recruits, kinesin-1 motor to drive the anterograde motility of late endosome/lysosome (LE/Lys) on microtubule tracks (Keren-Kaplan and Bonifacino, 2021; Rosa-Ferreira and Munro, 2011). Interestingly, co-expression of RUFY3 caused a striking shift in Arl8b distribution to the perinuclear region wherein both proteins colocalized on these perinuclear compartments (see inset, **Fig. 2G**; Pearson's and Mander's colocalization coefficients shown in **Fig. 2J-K**). Consistent with our analysis of the residues of RUFY3 required for Arl8b binding, no significant colocalization or a change in Arl8b distribution was observed in cells expressing RUFY3 (Δ446–561) and RUFY3 (RK→A) mutants (**Fig. 2H-I**; Pearson's and Mander's colocalization coefficients shown in **Fig. 2J-K**). Thus, our data suggest that RUFY3 is an Arl8b interaction partner that promotes the perinuclear positioning of lysosomes.

RUFY3 is essential and sufficient to drive perinuclear lysosome positioning

We used two independent strategies to corroborate whether RUFY3 is essential and sufficient to drive LE/Lys perinuclear positioning. Using the RNA interference approach (siRNA and shRNA), we depleted RUFY3 in HeLa cells and analyzed lysosome distribution. The efficiency of RUFY3 silencing was found to be > 90%, as confirmed by Western blotting (**Fig. 3A** and **Supplementary Fig. S3A**). Consistent with our results that RUFY3 expression promotes perinuclear clustering of lysosomes, RUFY3 depletion by either siRNA or shRNA had the opposite effect, i.e. lysosomes were now localized to the cell periphery (**Fig. 3B-C**; **Fig. 3E** and quantification is shown in **Fig. 3F**; **Supplementary Fig. S3B-D**). The peripheral lysosomal distribution was rescued in cells expressing siRNA-resistant RUFY3 construct, indicating that the phenotype was specifically due to RUFY3 depletion and not due to the off-target effect of siRNA oligos (**Fig. 3D-E**; quantification is shown in **Fig. 3G**). RUFY3 depletion in other cell types, including ARPE-19 (retinal pigment epithelial cells), U2OS (osteosarcoma cells), and A549 (lung adenocarcinoma cells), showed a similar distribution of lysosomes towards the cell periphery (**Supplementary Fig. S3E-G**). Notably, we also found that RUFY3-depleted cells had a ~ 1.3-fold increase in their surface area compared to control siRNA or shRNA treated cells (**Supplementary Fig. S3H-I**). Interestingly, cell spreading is reduced upon Myrlysin gene knockout, where lysosomes are clustered in the perinuclear region (Pu et al., 2015). In contrast, the surface area of cells is increased upon dynein depletion (Rishal et al., 2012), where lysosomes, similar to RUFY3 depletion, are localized to the cell periphery. These observations suggest that lysosome distribution might regulate cell spreading, but the mechanistic basis of how this is achieved remains unclear.

Next, we used the knockout-sideways approach to test whether the presence of RUFY3 on the organelle membrane was sufficient to drive their positioning to the perinuclear region. To this end, we used the FRB-FKBP rapamycin-induced heterodimerization system to mislocalize RUFY3 to mitochondria (where it is not present under endogenous conditions) and analyzed mitochondria distribution (**Fig. 3H**). As expected, we found mitochondrial localization of FKBP-GFP (vector transfected) and FKBP-GFP-RUFY3 fusion protein in the presence of rapamycin and not in untreated cells (**Fig. 3I**). Notably, in the presence of rapamycin, RUFY3-transfected cells showed a dramatic clustering of mitochondria in the perinuclear region. In contrast, vector-transfected cells showed typical mitochondrial distributions (compare second and fourth panel, **Fig. 3I**). Quantification of mitochondrial intensity distribution showed increased perinuclear index in cells expressing FKBP-GFP-RUFY3 in the presence of rapamycin (**Fig. 3J**). Taken together, we conclude that RUFY3 localization to the organelle membrane is sufficient to drive their distribution to the perinuclear region.

RUFY3 recruits the JIP4-dynein-dynactin complex to mediate retrograde transport of lysosomes

To investigate the RUFY3 mode of action, we performed a GST-pulldown assay with GST-RUFY3 as a bait protein to identify potential interaction partners. Interestingly, in the GST-RUFY3 eluate, we found peptides corresponding to cytoplasmic dynein heavy chain (DYNC1H1/DHC); dynactin 1/p150^{glued} (DCTN1), a subunit of dynactin complex that mediates dynein activation, and peptides of JIP4/SPAG9 scaffolding protein that interact with dynein/dynactin and link dynein to the organelle membranes (**Fig. 4A** and

Supplementary Table I) (Reck-Peterson et al., 2018; Willett et al., 2017). We confirmed the mass spectrometric data by immunoprecipitating endogenous RUFY3 and probing for JIP4 and vice versa. Dynein and dynactin subunits were also co-immunoprecipitated in the RUFY3-JIP4 complex (**Fig. 4B-C**). To test whether RUFY3 recruits JIP4 to Arl8b-positive lysosomes, we analyzed JIP4 localization in cells either expressing Arl8b alone or co-expressing both Arl8b and RUFY3. We found enhanced colocalization of Arl8b and JIP4 in the presence of RUFY3 (**Fig. 4D-E**). Recruitment of $p150^{glued}$ dynactin subunit to Arl8b-positive structures was also increased in cells co-expressing RUFY3 (**Supplementary Fig. S4A-B**). In agreement with these immunofluorescence observations, immunoprecipitation data confirmed that JIP4 interaction with Arl8b was dependent upon RUFY3 expression levels (**Fig. 4F-G**). We next tested whether dynein and JIP4 are required for RUFY3-mediated perinuclear clustering of lysosomes. RUFY3 overexpression failed to cause perinuclear clustering of lysosomes in JIP4- or dynein-depleted cells, suggesting that the JIP4-dynein motor complex is required for RUFY3-mediated perinuclear lysosome positioning (**Fig. 4H-I**; quantification is shown in **Fig. 4J**; **Supplementary Fig. S4C-D**).

These conclusions led to a hypothesis that RUFY3 recruits dynein motor on lysosomes and thereby mediate dynein-dependent lysosomal perinuclear positioning. Indeed, the motility behavior of lysosomes analyzed by tracking individual lysosomes showed that similar to dynein depletion, RUFY3 depletion significantly increased the total mobile fraction and the average speed of individual lysosomes (**Fig. 5A-C**; see **Supplementary Movies S1-3**; quantification is shown in **Fig. 5D-E**). Thus, our data suggest that upon RUFY3 and/or dynein depletion, there is an increase in the proportion of mobile lysosomes. To directly analyze whether RUFY3 regulates dynein subunit levels on lysosomes, we used density gradient ultracentrifugation to isolate lysosomes from control and RUFY3-depleted cells. Indeed, upon RUFY3 depletion, dynein intermediate chain (DIC) levels were reduced in the lysosomal fractions compared to the control cells (**Fig. 5F**). Finally, based on our hypothesis, we predicted that the expression of another lysosomal dynein adaptor in RUFY3-depleted cells should reinstate dynein levels on lysosomes, reflected by a change in lysosome distribution from the periphery to the perinuclear region. Indeed, RILP and TMEM55B, both of which interact with and recruit dynein-dynactin on the LAMP1 compartment (Jordens et al., 2001; Willett et al., 2017), could reposition lysosomes to the perinuclear region in RUFY3-depleted cells (compare untransfected with transfected cells, **Fig. 5G-I**; quantification is shown in **Fig. 5J**). Taken together, our results show that RUFY3 is an Arl8b effector that recruits dynein on lysosomes to maintain the typical stable pool of immobile lysosomes localized in the perinuclear region of the cell.

Depletion of RUFY3 reduces lysosome size

Previous studies have shown that the perinuclear and the peripheral pools of lysosomes have few differential characteristics and functions wherein the peripheral pool of lysosomes is more poised for crosstalk and fusion with the plasma membrane and serum-dependent-mTORC1 activation (Jia and Bonifacino, 2019; Korolchuk et al., 2011; Pu et al., 2017). In contrast, the perinuclear lysosomal subpopulation is more suited for interaction with perinuclear late endosomes/autophagosomes and, subsequently, cargo degradation (Kimura et al., 2008). Moreover, in at least one study, it has been reported that the peripheral pool of lysosomes is less acidic and less accessible to biosynthetic cargo

(such as cathepsins) (Johnson et al., 2016). However, a subsequent report has shown that peripheral and perinuclear lysosomes have a similar pH (~ 4.4) (Ponsford et al., 2020).

Since RUFY3 depletion results in an increased lysosomal pool near the plasma membrane, we wanted to determine whether lysosome characteristics including, their pH, size and number, are altered in these cells. We used fluorescent dyes-Lysotracker and Lysosensor Yellow/blue DND-160, which have different characteristics but share the property of fluorescing in acidic compartments (Ma et al., 2017). Intensity variations in Lysotracker staining report on the size and number of acidic compartments but cannot report variations in pH within the acidic range (Guha et al., 2014). Lysosensor dyes are pH sensitive used for ratiometric measurement of intraorganellar pH of acidic organelles (Diwu et al., 1999). Interestingly, while we did not observe any significant changes in lysosome pH in RUFY3-depleted cells (5.63 ± 0.19), as compared to control cells (5.49 ± 0.18) (**Fig. 6A-B**), there was a two-fold reduction in lysotracker intensity in RUFY3-depleted cells, as compared to control (**Fig. 6C-D**).

To assess the average size of lysosomes, we quantified the area of lysotracker-labeled vesicles in control and RUFY3-depleted cells (**Fig. 6E-G**). As shown in **Fig. 6H**, the average area of lysosomes per cell was reduced by ~ 30% upon RUFY3 depletion, as compared to control. The decrease in lysosome size upon RUFY3 depletion (as reflected by lysotracker intensity) was rescued in cells expressing RUFY3 siRNA-resistant construct, indicating that change in lysosome size is specifically due to RUFY3 depletion (**Fig. 6G**; quantification is shown in **Fig. 6H-I**). Moreover, we also found a ~ 2-fold increase in the number of lysotracker-positive lysosomes in RUFY3-depleted cells, which, as previously reported (Vogel et al., 2015; Yordanov et al., 2019), could be a potential mechanism for cells to compensate for the reduced lysosome size (**Fig. 6J**).

Next, we analyzed the ultrastructure of LE/Lys by transmission electron microscopy imaging on thin sections of control and RUFY3-depleted cells. As compared to control, lysosomes appeared to be smaller, denser and more numerous upon RUFY3 depletion (see insets, **Fig. 6K-L**). The diameter of lysosomes was reduced by ~ 20% in RUFY3-depleted cells compared to control, which would translate into a ~ 50% reduction in lysosome volume (**Fig. 6M**) (Yordanov et al., 2019). Here also, we noted that lysosome numbers were increased with on average 8 lysosomes (multi-lamellar structures) visible in control micrographs while typically 11 were present in micrographs from RUFY3-depleted cells (**Fig. 6N**).

Silencing of retrograde transport machinery components reduces lysosome size and increases fission events

Kinesin and dynein motor proteins are thought to create a tug-of-war to pull the organelle membranes in opposite directions. Thus, processes such as tubulation and membrane fission are regulated by motor activity (Du et al., 2016; Li et al., 2016; Soppina et al., 2009). We hypothesized that the optimal presence of motor proteins and their recruiting factors (such as RUFY3) is required for maintaining the normal size distribution of lysosomes. Indeed, as upon RUFY3 knockdown, lysosomes were smaller and more numerous in dynein- and JIP4-depleted cells (see inset, **Fig. 7A-D**; quantification is shown in **Fig. 7E-F**). Moreover, lysosome size measured as a function of lysotracker intensity was reduced in dynein- and

JIP4-depleted cells (**Fig. 7G**). The decrease in lysotracker was similar to what we had previously observed in RUFY3-depleted cells. Notably, there was no additional decrease in lysotracker intensity when RUFY3 and dynein were knocked down together compared to cells treated with RUFY3 siRNA (**Fig. 7H**), suggesting that RUFY3 influence on lysosome size is likely by its ability to recruit dynein on lysosomes. We also tested whether a decrease in lysosomal size in RUFY3 knockdown is because of reduced incoming cargo transport to lysosomes. To this end, we pre-labeled lysosomes in control and RUFY3-depleted cells using Alexa-Fluor 568-conjugated dextran and incubated these cells with Alexa-Fluor 488-conjugated dextran for different time points. As shown in **Supplementary Fig. S5A-D**, we did not find any significant change in the colocalization of the dextran conjugates upon RUFY3 depletion, suggesting that fusion of cargo-laden late endosomes with terminal lysosomes is not affected by RUFY3 depletion.

Finally, to test whether tubulation and/or fission events from lysosomes are altered upon RUFY3 depletion, we quantified the number of membrane fission events from vesicles marked by LAMP1-GFP in control and RUFY3 depletion. In control cells, of the 66 LAMP1-GFP endosomes imaged for typically 4 min, we observed 84 membrane fission events (representative example of time-lapse of a fission event shown in **Fig. 7I** (see **Supplementary Movie S4**) and quantification is shown in **Fig. 7K**). In RUFY3-depleted cells, we found a ~ 1.5 to 2-fold increase in fission events with 70 LAMP1-GFP endosomes undergoing 140 fission events (representative example of time-lapse of a fission event shown in **Fig. 7J** (see **Supplementary Movie S5**) and quantification is shown in **Fig. 7K**). The newly formed terminal lysosomes have been shown in previous work to be less degradative, based on the lack of fluorescence signal of cleaved cathepsin substrate (Magic Red) in these compartments (Cheng et al., 2018; Johnson et al., 2016). By performing SIM imaging, we noted an increase in Magic Red^{-}/$LAMP1^{+}$ population primarily localized at the cell periphery in RUFY3-depleted cells as compared to control cells, indicating that this population is likely the newly formed terminal lysosomes (see inset in **Supplementary Fig. S5E-F**; yellow arrowheads denote Magic Red^{-}/$LAMP1^{+}$ lysosomes). Finally, we assumed that inhibition or depletion of factors required for lysosomal reformation would restore the normal lysosomal size in RUFY3-depleted cells. Indeed, cells depleted of both RUFY3 and PIKFYVE enzyme, which is required for lysosomal tubulation, an event that occurs before fission (Choy et al., 2018; Saffi and Botelho, 2019; Sharma et al., 2019), restored the normal size distribution of lysosomes (see inset in **Fig. 7L-N**; quantification is shown in **Fig. 7O**). Taken together, our findings indicate that RUFY3-dependent dynein recruitment on lysosomes is crucial to maintain the perinuclear lysosomal pool, which, if disrupted, can result in excessive fission of lysosomes and their movement to the cell periphery, both likely due to an imbalance of forces exerted by the kinesin motor.

RUFY3 regulates nutrient-dependent lysosome repositioning but not autophagic cargo clearance

Previous reports have shown that Arl8b and its upstream regulator-BORC complex regulate nutrient-dependent lysosome positioning to the cell periphery (Pu et al., 2017; Pu et al., 2015). Based on our findings that RUFY3 functions as a dynein adaptor on lysosomes, we expected that RUFY3-depleted cells would fail to show repositioning of lysosomes to the perinuclear region in nutrient-starved cells. Indeed,

lysosomes continued to localize at the cell periphery in RUFY3-depleted cells that were subjected to either complete starvation (EBSS-media lacking both serum factors and amino acids) or serum starvation (DMEM-FBS) or only amino acid (DMEM-AA) (**Fig. 8A-D**). This was in contrast to the control siRNA treated cells, where as expected, lysosomes were accumulated in the perinuclear region in all three conditions of starvation (**Fig. 8A-D**; quantification is shown in **Fig. 8G**).

Lysosome clustering to the perinuclear region in nutrient-deprived cells has been shown to result in the enhanced propensity of fusion with mature autophagosomes, which is important for replenishing the macromolecular building blocks in the starved cells (Kimura et al., 2008). The fusion of autophagosomes and lysosomes and the degradation of autophagic cargo have classically been measured by the amount of autophagosomal protein LC3B remaining in the cells with/without starvation (Klionsky et al., 2021). To address the RUFY3 role in autophagic cargo degradation, we assessed the amount of lipidated LC3 (LC3B-II) levels in fed and starved cells treated with control or RUFY3 siRNA. As shown in **Fig. 8E**, while the initial levels of LC3B-II were modestly less in the fed state upon RUFY3 depletion, upon EBSS treatment, both control and RUFY3-depleted cells showed a similar increase in LC3B-II levels. Also, LC3B-II levels were rescued to a similar extent in control and RUFY3-depleted cells treated with Bafilomycin A1 (BafA1), an inhibitor of lysosomal acidification and, therefore, degradation (**Fig. 8F**). These results suggest that RUFY3 does not regulate autophagosome-lysosome fusion. To corroborate the autophagy flux analysis, we also measured the colocalization between LC3 and LAMP1 in serum-starved-control and -RUFY3-depleted cells treated with BafA1 to ensure the maximal frequency of autolysosomes is observed in these experiments. While there was a modest decrease in the LC3/LAMP1 colocalization in RUFY3-depleted cells, the difference in average Pearson correlation coefficient values from control was minor and not significant (**Fig. 8H-I**; quantification is shown in **Fig. 8J**). We noted that several of the peripheral lysosomes in RUFY3-depleted cells were also colocalized with LC3, suggesting that autolysosome formation is also occurring outside the perinuclear region (see inset in **Fig. 8I**). Thus, while lysosome repositioning to the perinuclear subcellular location was strikingly reduced upon RUFY3 depletion, no significant changes in autophagosome-lysosome fusion and LC3 flux were observed in RUFY3-depleted cells. Our findings agree with previous work showing that peripheral lysosomes can also undergo fusion with autophagosomes (Jia et al., 2017). Next, we also assessed the degradation of EGFR, which in complex with its ligand EGF traffics to the lysosome for degradation (Khatter et al., 2015a). To this end, we pulsed control and RUFY3-depleted cells with EGF for increasing time duration and monitored the remaining EGFR levels in total cell lysates. As shown in **Supplementary Fig. S6A**, degradation of EGFR was observed in RUFY3-depleted cells. As compared to control cells, there was a modest increase in EGFR degradation rate upon RUFY3 knockdown (quantification is shown in **Supplementary Fig. S6B**).

We next investigated whether selective autophagy of particular cellular cargo was altered in RUFY3-depleted cells. To this end, we tested the autophagic clearance of protein aggregates induced by puromycin in control and RUFY3-depleted cells. After 2 hr of puromycin incubation, several protein aggregate punctae marked by the presence of autophagy adaptor p62 and ubiquitin (Ub) were evident in control cells (upper panel, **Fig. 8K**; quantification is shown in **Fig. 8M**). In contrast, we found a striking decrease in the formation of these aggregated punctae upon RUFY3 depletion (lower panel, **Fig. 8K**;

quantification is shown in **Fig. 8M**). This phenotype is mainly reminiscent of dynein inhibition or depletion, as the formation of visible protein aggregates and eventually into a large aggresome structure requires dynein-dynactin function (Johnston et al., 2002). Indeed, the phenotype of dynein-and JIP4-depleted cells at 2 hr of puromycin treatment was strikingly similar to RUFY3 depletion (**Supplementary Fig. S6C-D**). After 8 hr of puromycin treatment, the size of $p62^+/Ub^+$ aggregates was expectedly increased; their location was in the perinuclear region, and a consequent reduction in the number of protein aggregates was observed in control cells (upper panel, **Fig. 8L**; quantification is shown in **Fig. 8M**). In contrast, RUFY3-depleted cells showed a ~ 2-fold increase in the number of $p62^+/Ub^+$ aggregates and a substantial decrease in the size of aggresome-like structures (lower panel, **Fig. 8L**; quantification is shown in **Fig. 8M**). Notably, in RUFY3-depleted cells, these aggregates were dispersed throughout the cytosol instead of their characteristic perinuclear location (compare the upper and lower panels of **Fig. 8L**). We also assessed the clearance of $p62^+/Ub^+$ aggregates induced by 2 hr puromycin treatment followed by a wash and incubation in complete media for 3 hr and 6 hr (**Supplementary Fig. S6E**). The clearance of $p62^+/Ub^+$ aggregates was similar in both control and RUFY3-depleted cells, suggesting that RUFY3 regulates the formation but not clearance of the selective autophagy cargo (**Fig. 8F-I**).

Discussion

The small G protein Arl8b is a crucial player regulating lysosomal positioning and functions in the subcellular space (Khatter et al., 2015b). Arl8b overexpression was shown to increase the proportion of lysosomes undergoing bi-directional long-range movement on the microtubule tracks (Hofmann and Munro, 2006). Subsequent studies revealed that Arl8b binds to effector protein PLEKHM2 (also known as SKIP), which in turn binds and recruits kinesin-1 motor to promote anterograde motility of lysosomes (Keren-Kaplan and Bonifacino, 2021; Pu et al., 2015; Rosa-Ferreira and Munro, 2011; Tuli et al., 2013). However, it was not known whether Arl8b could mediate long-range retrograde movement of lysosomes. In this study, we have identified RUFY3 as an Arl8b effector that recruits the JIP4-dynein-dynactin complex to mediate the retrograde motility of lysosomes.

Among the six transcript variants of RUFY3 annotated on NCBI, only variant 2 (469 amino acids long) is functionally characterized and shown to regulate axon guidance in neurons and migration of cancer cells, processes that depend on actin cytoskeletal dynamics (Honda et al., 2017; Kitagishi and Matsuda, 2013; Mori et al., 2007; Wang et al., 2015; Wei et al., 2014). This study presents evidence that the longest transcript variant of RUFY3, variant 1 (620 amino acids long), localizes to lysosomes and regulates lysosome positioning. Variant 1 binds to Arl8b via a sequence in its C-terminal region (amino acids 441–561), which is not present in other variants, except for variant 4. Thus, the localization and function of RUFY3 variants may differ from each other based on certain sequence features. As effectors such as PLEKHM1 and PLEKHM2 bind to Arl8b via their RUN domains (Marwaha et al., 2017), it was surprising to find that the RUN domain of RUFY3 was not required for binding to Arl8b. Future work is needed to elucidate what determines the binding of some, but not all, RUN domains to Arl8b.

RUFY3 joins the league of other late endosomal/lysosomal proteins, including RILP, TRPML1, TMEM55B and SEPT9, which interact with dynein-dynactin retrograde motor either directly or via binding to dynein adaptors JIP3 or JIP4 (Jordens et al., 2001; Kesisova et al., 2021; Li et al., 2016; Willett et al., 2017). This list raises a question as to why several dynein adaptors are required for lysosomal motility (**Fig. 9A**). One explanation could be that multiple adaptors are required to engage a sufficient number of dynein motors to win the tug-of-war against kinesin, which generates force equivalent to eight dynein-dynactin complexes (Soppina et al., 2009) (**Fig. 9A (I)**). A second explanation could be that different adaptors are required under different physiological conditions; for instance, one or more lysosomal dynein adaptors might be required specifically under conditions such as starvation or oxidative stress where lysosomes are clustered in the perinuclear region (**Fig. 9A (II)**). Indeed, expression of lysosomal adaptor TMEM55B is under the control of transcription factors TFEB, TFE3, and SREBF2, activated upon starvation and stress due to cholesterol accumulation in the lysosomal lumen, respectively (Willett et al., 2017). Additionally, phosphorylation of TMEM55B by ERK/MAPK regulates lysosome positioning (Takemasu et al., 2019). A third reason could be that while markers like LAMP1 are common, but different dynein adaptors are essentially required for the motility of distinct compartments (**Fig. 9A (III**). Indeed, recent studies have suggested that there are LAMP1-positive compartments that are non-degradative, as well as differences in pH and cathepsin activity have been documented between perinuclear and peripheral lysosomes enriched for Rab7 and Arl8b, respectively (Cheng et al., 2018; Johnson et al., 2016). Thus, Rab7 effector-RILP is likely to be the adaptor of choice for late endosomal perinuclear compartments. At the same time, RUFY3 is likely to be a dynein adaptor for compartments enriched for the small G protein Arl8b.

While RUFY3 was required for the organization of the lysosome population at the whole-cell scale, surprisingly, its depletion also affected the characteristics of individual lysosomes, namely lysosome size. We found that average lysosome volume was reduced by a significant value of almost 50% upon RUFY3 depletion. As noted in earlier studies (Choy et al., 2018; Yordanov et al., 2019), a reduction in lysosome size is accompanied by an increase in lysosome number that was also observed upon RUFY3 depletion. Thus, a significant proportion of lysosomes in RUFY3 knockdown were smaller, numerous and localized in the peripheral subcellular space. The average velocity of individual lysosomes was increased upon RUFY3 depletion, possibly because the lysosome size was reduced and/or kinesin-mediated forces were dominant on lysosomes (**Fig. 9B**).

Is there a common explanation that underlies RUFY3 role in regulating both the positioning and size of lysosomes? We speculate that in RUFY3 knockdown, lysosomes escape more frequently from the perinuclear cloud and move in a kinesin-dependent manner on the microtubule highway. The dominant kinesin-dependent forces in RUFY3-depleted cells promote lysosome tubulation and fission, a process that also requires PIKFYVE-mediated PtdIns(3,5)P2 and can be inhibited by PIKFYVE depletion. In accordance with our hypothesis, depletion of dynein and JIP4 also reduces the size of individual lysosomes and cause peripheral positioning of the lysosome population. Consequently, these numerous proteolytic lysosomes outside the perinuclear cloud might be disruptive to the usual temporal kinetics of cargo degradation, as an encounter of nascent endosomes/autophagosomes with lysosomes will be more frequent under such conditions.

Future studies will establish whether the correlation between lysosome positioning and size reflects different biogenesis stages of this enigmatic organelle. Our study suggests one model wherein new lysosomes emerge at the cell periphery, and as lysosomes are subjected to dynein forces, they become clustered in a perinuclear pool poised for fusion with incoming cargo vesicles.

Materials And Methods

Cell Culture and RNAi

HeLa, HEK293T, U2OS and A549 cells (from ATCC) were maintained in DMEM media (Lonza) supplemented with 10% FBS (Gibco) at 37°C with 5% CO_2 in a humidified cell culture chamber. For culturing ARPE-19 cells (from ATCC), DMEM/F-12 media (Gibco) supplemented with 10% FBS was used. Serum starvation was performed by incubating cells in DMEM with 2 mM L-glutamine for 1 hr. Combined amino-acid and serum starvation was performed by incubating cells in EBSS for 4 hr. Amino-acid starvation was performed by incubating cells in amino-acid-free DMEM (US Biologicals) supplemented with 10% dialyzed-FBS (Gibco) for 4 hr. Each cell type was regularly screened for the absence of mycoplasma contamination by using the MycoAlert Mycoplasma Detection Kit (Lonza) and was cultured for no more than 15 passages.

For gene silencing, siRNA oligos or SMARTpool were purchased from Dharmacon and prepared according to the manufacturer's instructions. Following siRNA oligos were used in this study: control siRNA, TGGTTTACATGTCGACTAA; RUFY3 siRNA, GATGCCTGTTCAACAAATGAA; JIP4 siRNA, GAGCATGTCTTTACAGATC; DHC siRNA, GAGAGGAGGTTATGTTTAA; PIKFYVE siRNA, ON-TARGETplus SMARTpool (L-005058-00-0005). For shRNA mediated gene silencing, control shRNA (SHC016) and RUFY3 shRNA (TRCN0000127915) were purchased from Sigma-Aldrich. Transient transfection of siRNAs was performed with DharmaFECT 1 (Dharmacon) according to the manufacturer’s instructions.

For shRNA-mediated gene silencing, lentiviral transduction was performed as described previously (Garg et al., 2011). Briefly, for lentiviral transduction, HeLa cells were plated at 100,000/well in 6-well plates (Corning) in 8 µg/mL Polybrene (Sigma-Aldrich) and transduced by addition of 100 µL viral supernatant. 24 hr later, puromycin (Sigma-Aldrich) was added at 3 µg/mL to select transductants and experiments performed on Days 5–21 following transduction.

Mammalian Expression Constructs

All the expression plasmids used in this study are listed in **Supplementary Table II**.

Antibodies and Chemicals

All the antibodies used in this study are listed in **Supplementary Table III**. Alexa-Fluor-conjugated-Dextran, LysoTracker dye, LysoSensor dye, EGF, Phalloidin, and DAPI were purchased from Invitrogen. Polybrene, Puromycin, EBSS and Bafilomycin A1 were purchased from Sigma-Aldrich. The Magic Red Cathepsin B Kit was purchased from Bio-Rad.

Transfection, Immunofluorescence and Live-Cell Imaging

Cells grown on glass coverslips (VWR) were transfected with desired constructs using X-treme GENE-HP DNA transfection reagent (Roche) for 16–18 hr. Cells were fixed in 4% PFA in PHEM buffer (60 mM PIPES, 10 mM EGTA, 25 mM HEPES and 2 mM $MgCl_2$ and final pH 6.8) for 10 min at room temperature (RT). Post-fixation, cells were incubated with blocking solution (0.2% saponin + 5% normal goat serum (NGS) in PHEM buffer) at RT for 30 min, followed by three washes with 1XPBS. Following the blocking step, cells were incubated with primary antibodies in staining solution (PHEM buffer + 0.2% saponin + 1% NGS) for 1 hr at RT, washed three times with 1XPBS and then incubated for 30 min at RT with Alexa-fluorophore-conjugated secondary antibodies in staining solution. Coverslips were mounted using Fluoromount G (Southern Biotech), and confocal images were acquired using Carl Zeiss 710 Confocal Laser Scanning Microscope with a Plan Apochromat 63×/1.4 NA oil immersion objective and high-resolution microscopy monochrome cooled camera AxioCamMRm Rev. 3 FireWire (D) (1.4 megapixels, pixel size 6.45 µm × 6.45 µm). ZEN Pro 2011 (ZEISS) software was used for image acquisition. All images were captured to ensure that little or no pixel saturation is observed. The representative confocal images presented in figures were processed and adjusted for brightness and contrast using Fiji software (Schindelin et al., 2012) or Adobe Photoshop CS.

For live-cell imaging experiments, cells were seeded on glass-bottom tissue culture treated cell imaging dish (Eppendorf). For vesicle tracking experiments, cells were pulsed with Alexa-Fluor 488-conjugated dextran (Invitrogen) for 16–18 hr and then the cells were washed once with 1XPBS and further chased for 6 hr in phenol red-free media (Gibco). Live-cell imaging was performed using a Zeiss LSM 710 confocal microscope equipped with an environmental chamber set at 37°C and 5% CO_2.

Structured Illumination Microscopy (SIM)

For SIM imaging, cells were processed, fixed and stained as described previously. SIM images were captured with Zeiss ELYRA 7 (Lattice SIM Technology) using either Plan Apo 40×/1.40 oil or Plan Apo 63×/1.40 oil objective and sCMOS camera (PCO Edge). A lattice pattern structured samples, and 15 phases shifted raw images were acquired for every Z plane with a slice size of 110 nm. The complete system control, imaging and processing of raw image files to final super-resolution images were done using the SIM module of the Zen Black software (Carl Zeiss MicroImaging).

Time-lapse SIM imaging was performed using the climate control stage, incubation system, and Plan Apo 40×/1.40 oil objective to visualize fission events. Movies were recorded for a period of ~ 4 min with 1.4 frames per sec.

To visualize $LAMP1^+$/Magic Red^- vesicles, SIM imaging was performed on live-cells after incubating the cells with Magic Red Cathepsin B substrate (1:25 dilution, Bio-Rad) just before imaging. All representative SIM images were processed and adjusted for brightness and contrast using Fiji software or Adobe Photoshop. Imaris (Bit-plane) was used for making the isosurface view of the selected region of interest (ROI).

Image Analysis and Quantification

Lysosome distribution

To quantify the distribution of lysosomes (based on LAMP1 signal intensity), Fiji software was used. A boundary was drawn along the periphery of each selected cell using the “freehand” selection tool. With the “clear outside” function of Fiji software, removed LAMP1 signals from nearby cells. Next, an ROI was drawn around the nucleus (using DAPI fluorescence signal), and LAMP1 signal intensity was measured for that section. The same ROI was then incremented by 5 μm till the cell periphery, and LAMP1 intensity was measured for each incremented ROI. Finally, LAMP1 intensity was calculated for perinuclear (0–5 μm; by subtracting the intensity of 1st ROI from 2nd) and periphery (> 15 μm; by subtracting the intensity of 4th ROI from total cell intensity) region of cell as shown in Fig. 2D. LAMP1 distribution was plotted by dividing the each section’s intensity (perinuclear and periphery) with whole-cell LAMP1 intensity. The same methodology was employed for quantifying mitochondria distribution (based on TOM-20 signal intensity) from images presented in Fig. 3I.

Analysis of LysoTracker vesicles

To quantify the area, count and intensity of LysoTracker-positive vesicles, captured field images were analyzed using the “MaxEntropy” threshold and “Particles Analyze” functions of Fiji software.

Analysis of LAMP1-positive vesicles

To measure the area and number of LAMP1-positive vesicles from SIM images, Z stacks of each micrograph was converted to 8-bit “Max Intensity Projection” using Fiji software. Using the “Analyze Particle” tool with the “Otsu” threshold was used for calculating the area and number. For TEM micrographs, the diameter of individual lysosome was measured manually by drawing a straight line across the lysosome using the “Line” tool in Fiji software.

Surface area analysis

The surface area of cells was quantified manually by drawing the periphery of the cell (using Phalloidin staining) using the “freehand” and “Measure Function” tools in Fiji software.

Quantification of lysosomal fission events

To quantify fission events from SIM time-lapsed 2D images, all micrographs were converted into 8-bit gray-scale (for better visualization) and processed using the “Smooth Function” in the Fiji software. Next, non-overlapping ROI (about 5 in number) of the same dimensions were selected from different sections of each cell. From each ROI, distinctly located/ visible LAMP1-positive vesicles were selected and observed one by one in all the frames for fission events, i.e. formation of new LAMP1-positive vesicle from the parent vesicle. In this analysis, all the clustered or tethered LAMP1-positive vesicles were excluded.

Colocalization analysis

For all the colocalization analysis, the JACoP plugin of Fiji software was used to determine Pearson's correlation coefficient and Mander's overlap.

Single-particle Tracking

To perform single-particle tracking analysis of lysosomes, cells were pulsed with Alexa-Fluor 488-conjugated Dextran (Invitrogen) for 12 hr. Cells were washed once with 1XPBS and further incubated for 8 hr in phenol red-free DMEM. Time-lapse confocal imaging was done as discussed above. To measure mobile fraction and the average speed of lysosomes from time-lapsed images, "TrackMate" plugin (Tinevez et al., 2017) of Fiji software was used with following parameters:

- Vesicle diameter, 1 µm

- Detector, DoG

- Initial thresholding, none

- Tracker, Simple LAP tracker

- Linking max distance, 2 µm

- Gap-closing max distance, 2 µm

- Gap-closing max frame gap, 2

- Filters, none

Cell lysates, Co-immunoprecipitation and Immunoblotting

For preparing lysates, cells were lysed in ice-cold RIPA lysis buffer (10 mM Tris-Cl (pH 8.0), 1 mM EDTA, 0.5 mM EGTA, 1% Triton X-100, 0.1% SDS, 0.1% sodium deoxycholate, 140 mM NaCl supplemented with phosphostop (Roche) and protease inhibitor cocktail (Sigma-Aldrich)). The samples were incubated on ice for 2 min followed by vortexing for 30 sec, and this cycle was repeated a minimum of five times and subjected to centrifugation at 13,000 rpm for 10 min 4°C. The clear supernatants were collected, and protein amounts were quantified using the BCA kit (Sigma-Aldrich).

To perform co-immunoprecipitation, cells were lysed in ice-cold TAP lysis buffer (20 mM Tris pH 8.0, 150 mM NaCl, 0.5% NP-40, 1 mM $MgCl_2$, 1 mM Na_3VO_4, 1 mM NaF, 1 mM PMSF and protease inhibitor cocktail). The lysates were incubated with indicated antibody conjugated-agarose beads at 4°C rotation for 3 hr, followed by four washes with TAP wash buffer (20 mM Tris pH 8.0, 150 mM NaCl, 0.1% NP-40, 1 mM $MgCl_2$, 1 mM Na_3VO_4, 1 mM NaF and 1 mM PMSF). The samples were then loaded on SDS-PAGE for further analysis.

For immunoblotting, protein samples separated on SDS-PAGE were transferred onto PVDF membranes (Bio-Rad). Membranes were blocked overnight at 4°C in blocking solution (10% skim milk in 0.05% PBS-Tween 20). Indicated primary and secondary antibodies were prepared in 0.05% PBS-Tween 20. The membranes were washed for 10 min thrice with 0.05% PBS-Tween20 or 0.3% PBS-Tween 20 after 2 hr incubation with primary antibody and 1 hr incubation with secondary antibody. The blots were developed using a chemiluminescence-based method (Thermo Scientific) using X-ray films (Carestream). To perform densitometry analysis of immunoblots, Fiji software was used.

Recombinant Protein Purification, GST-pulldown Assay and Mass Spectrometry Analysis

All GST-tagged proteins used in this study were expressed and purified in *E. coli* BL21 strain (Invitrogen). A single transformed colony was inoculated in Luria–Bertani broth containing plasmid vector antibiotic and incubated at 37°C in a shaking incubator for setting-up primary cultures. Following 8–12 hr of culturing, 1% of primary inoculum was used to set up secondary cultures and subjected to incubation at 37°C with shaking until absorbance of 0.6 at 600 nm was reached. For induction of protein expression, 0.3 mM IPTG (Sigma-Aldrich) was added to the cultures, followed by incubation for 16 hr at 16°C with shaking. Post-induction period, bacterial cultures were centrifuged at 6,000 rpm for 10 min, washed once with 1XPBS, and resuspended in lysis buffer (20 mM Tris and 150 mM NaCl, pH 7.4) containing protease inhibitor tablet (Roche) and 1 mM PMSF (Sigma-Aldrich). Bacterial cells were lysed by sonication, followed by centrifugation at 11,000 rpm for 30 min at 4°C. The clear supernatants were incubated with glutathione resin (Gbiosciences) on rotation for 1–2 hr at 4°C to allow GST binding and GST-tagged proteins. The beads were washed a minimum of six times with wash buffer (20 mM Tris, 300 mM NaCl, pH 7.4) to remove impurities.

For GST-pulldown experiments, cells were lysed in ice-cold TAP lysis buffer (20 mM Tris (pH 8.0), 150 mM NaCl, 0.5% NP-40, 1 mM $MgCl_2$, 1 mM Na_3VO_4, 1 mM NaF, 1 mM PMSF, and protease inhibitor cocktail), followed by incubation in ice for 10 min and centrifuged at 13,000 rpm for 10 min. Lysates were collected and incubated with GST or GST-tagged proteins bound to glutathione resin at 4°C for 3–4 hr with rotation. Following incubation, beads were washed a minimum of six times with TAP lysis buffer, and elution was done by boiling the samples in Laemmli buffer and subjected to SDS-PAGE for further analysis.

To search for proteins that bind to RUFY3, GST-pulldown assay with GST-RUFY3 and GST (as a control) using HEK293T cell lysates was performed as described above. The final eluate containing the protein of interest (RUFY3) and the proteins associated with it were identified by tandem mass spectrometry at the Taplin Mass Spectrometry Facility (Harvard Medical School, Boston, USA). The RUFY3 interactome data was filtered using CRAPOME tools (available at https://reprint-apms.org/) and is listed in **Supplementary Table I**.

Yeast two-hybrid Assay

Matchmaker Gold Yeast Two-Hybrid System (Clontech) was used as per the manufacturer's instructions for carrying out yeast two-hybrid screening. Briefly, human Arl8b cDNA cloned in GAL4-BD vector (pGBKT7) was used as bait. The bait plasmid transformed Y2HGold yeast strain was mated with Y187 strain transformed with human brain cDNA library. For small scale yeast two-hybrid assay, plasmids encoding GAL4-AD and GAL4-BD fusion encoding constructs were co-transformed in *Saccharomyces cerevisiae* Y2HGold strain (Clontech), streaked on plates lacking leucine and tryptophan (-Leu/-Trp) and allowed to grow at 30°C for three days. The co-transformants were replated on non-selective medium (-Leu/-Trp) and selective medium (-Leu/-Trp/-His) to assess interaction. All the drop-out yeast media was purchased from Takara.

Lysosome Immunoisolation

To immunopurify lysosomes, the “LysoIP” method (Abu-Remaileh et al., 2017) was used with some modifications. HEK293T cells stably expressing TMEM192-FLAG (control) or TMEM192-HA were collected and resuspended in ice-cold KPBS (136 mM KCl, 10 mM KH_2PO_4, adjusted to pH 7.25 with KOH) buffer and homogenized using dounce homogenizer (~ 20 strokes). The homogenized cells were gently collected and centrifuged for 2 min at 1000xg and the supernatant obtained after centrifugation was incubated with anti-HA antibodies-conjugated-agarose beads (Sigma-Aldrich) at 4°C for 15 min. Beads were gently washed thrice with KPBS, and bound lysosomes were eluted in Laemmli buffer and subjected to SDS-PAGE for further analysis.

Subcellular Fractionation

To perform lysosome enrichment, subcellular fractionation was carried using “Lysosome Enrichment Kit” (Thermo Scientific). Briefly, the cell pellet was resuspended in PBS and homogenized with a dounce homogenizer on ice (~ 20 strokes). To confirm cell lysis, microscopic examination of homogenate was done by adding 0.5% trypan blue dye. The homogenate was subjected to centrifugation at 500xg for 10 min at 4°C, and post-nuclear supernatant (PNS) was diluted in OptiPrep gradient media (Sigma-Aldrich) to a final concentration of 15% OptiPrep. The sample was then carefully overlayered on the top of a discontinuous density gradient (17%, 20%, 23%, 27%, 30%). The gradient was subjected to ultracentrifugation at 145,000xg in an SW60 Ti swinging bucket rotor (Beckman Coulter) for 4 hr at 4°C. After the spin, eight fractions of 400 µl each were collected from top to bottom. The fractions were spun again at 18000x g for 20 min in a SW41 Ti rotor at 4°C, and the resulting pellet was resuspended in 4X SDS-sample buffer, boiled for 10 min and analyzed by SDS-PAGE and immunoblotting.

Measurement of Lysosome pH

To measure the lysosome’s pH, LysoSensor Yellow/Blue DND-160 was used as described previously (Ma et al., 2017). Briefly, cells were trypsinized and incubated with 2 µM LysoSensor Yellow/Blue DND-160 (Invitrogen) for 3 min at 37°C in phenol red-free media. Cells were rinsed twice with 1XPBS to remove excess dye and incubated for 10 min in isotonic pH calibration buffers (143 mM KCl, 5 mM Glucose, 1 mM $MgCl_2$, 1 mM $CaCl_2$, 20 mM MES, 10 µM Nigericin and 5 µM Monensin) ranging from 4 to 6. Next, ~ 10,000 cells/well were distributed into a black 96-well plate (Thermo Scientific), and fluorescence reading

was recorded at 37°C using a 96-well plate multi-mode fluorescence reader (Tecan Infinite M-PLEX). Samples were excited at 340 nm and 380 nm wavelengths to detect emitted light at 440 nm and 540 nm, respectively. The pH calibration curve was generated by plotting the fluorescence intensity ratio of 340 nm to 380 nm against the respective pH value of buffers.

LysoTracker Red Uptake Analysis by Flow Cytometry

To quantify LysoTracker uptake, cells were incubated with 100 nM LysoTracker Red (LTR-DND-99; Invitrogen) for 1 hr in phenol red-free media (Gibco). Post-incubation period, LysoTracker-containing media was removed, and cells were trypsinized, washed and resuspended in ice-cold 1XPBS and analyzed by flow cytometry. Sample acquisition was done with BD FACS Aria Fusion Cytometer using BD FACS Diva software version 8.0.1 (BD Biosciences). Data analysis was done using BD FlowJo version 10.0.1.

Dextran Pulse-Chase Assay

Dextran pulse-chase assay to monitor cargo trafficking to lysosomes was performed as described previously (Garg et al., 2011). Briefly, lysosomes of RUFY3-silenced and control HeLa cells were labeled with Alexa-Fluor 546-conjugated-dextran (red) pulsed for 12 hr and then underwent an 8 hr chase to allow the accumulation in lysosomes. Cells were then incubated with a second dextran (Alexa-Fluor 488-conjugated-dextran; green) for 2 hr. The colocalization of both dextrans was assessed using the JACoP plugin of Fiji software.

EGFR Degradation Assay

RUFY3-silenced and control HeLa cells were serum-starved for 1 hr and incubated with 100 ng/mL EGF (Invitrogen) for the indicated time periods. After each time point, cells were processed for lysates preparation and immunoblotted with anti-EGFR antibody as described above. Densitometry analysis of EGFR band intensity normalized to GAPDH intensity was done using Fiji software.

Autophagy Flux Assay

Autophagic flux was determined by checking for the rescue of LC3B-II degradation by treating HeLa cells with V-ATPase inhibitor Bafilomycin A1 (100 nM; Sigma-Aldrich) steady-state or with serum starvation in EBSS for 2 hr. After treatment, cells were lysed using ice-cold RIPA buffer supplemented with protease inhibitor. An equal amount of lysates were loaded on SDS-PAGE, transferred to PVDF membrane and probed for LC3B-II and β-tubulin. Densitometry analysis of LC3B-II band intensity normalized to β-tubulin intensity was done using Fiji software.

Aggregate Formation and Clearance Assay

To induce the formation of protein aggregates, control and RUFY3-depleted HeLa cells growing on sterile coverslips were treated with 3 µg/mL puromycin (Sigma-Aldrich) for the indicated time period at 37°C. Post-treatment, cells were fixed and processed for immunofluorescence staining as described above.

For recovery/clearance assay, after induction of protein aggregates formation, cells were washed to remove puromycin, and fresh media is added for the indicated time period to allow clearance of protein aggregates. Post-treatment, cells were fixed and processed for immunofluorescence staining as described above.

To quantify the numbers of puromycin-induced protein aggregates, $p62^{+}/Ub^{+}$-punctae were counted using “Max Entropy” thresholding and “Analyze Particle” tools of Fiji software.

Transmission Electron Microscopy (TEM)

Sample processing and TEM was performed at the Harvard Medical School EM Facility (Boston, USA). Briefly, HeLa cells transfected with control siRNA or RUFY3 siRNA were fixed in routine fixative (2.5% glutaraldehyde/1.25% paraformaldehyde in 0.1 M sodium cacodylate buffer, pH 7.4) for 1 hr at RT and washed in 0.1 M sodium cacodylate buffer (pH 7.4). The cells were then postfixed for 30 min in 1% osmium tetroxide/1.5% potassium ferrocyanide, washed with water three times, and incubated in 1% aqueous uranyl acetate for 30 min, followed by two washes in water and subsequent dehydration in grades of alcohol (5 min each: 50, 70, 95, 2× 100%). Cells were removed from the dish in propylene oxide, pelleted at 3000 rpm for 3 min, and infiltrated overnight in a 1:1 mixture of propylene oxide and TAAB Epon (Marivac Canada). The samples subsequently embedded in TAAB Epon and polymerized at 60°C for 48 hr. The ultrathin sections were cut on a Reichert Ultracut-S microtome, picked up onto copper grids stained with lead citrate, and examined in a JEOL 1200EX transmission electron microscope. Images were recorded with an AMT 2k charge-coupled device camera.

Statistical Analysis

All graphs report the mean ± S.D., unless otherwise specified. *p* values were calculated using Student’s *t-test* from three independent biological replicates.

Data Availability

All data are contained within the manuscript.

Abbreviations

Alg2, Apoptosis-linked gene 2; Arl, Arf-like; Arl8b, Arf-like GTPase 8b; EGFR, Epidermal growth factor receptor; ER, Endoplasmic reticulum; FKBP, FK506-binding protein; FRB, FKBP–rapamycin binding domain; FYCO1, FYVE And Coiled-Coil Domain Autophagy Adaptor 1; GST, Gluathione-S-transferase; JIP4, C-Jun-amino-terminal kinase-interacting protein 4; LAMP1, Lysosomal-associated membrane protein 1; LE, Late endosome; LYS, Lysosome; MCOLN1, Mucolipin 1; mTORC1, mammalian target of rapamycin complex 1; PLEKHM1, Pleckstrin homology domain-containing family M member 1; PLEKHM2, Pleckstrin homology domain-containing family M member 2; RILP, Rab-interacting lysosomal protein; RUFY3, RUN and FYVE domain-containing protein family member 3; Sept9, Septin 9; shRNA, short hairpin RNA; SIM, Structured illumination microscopy; siRNA, short-interfering RNA; SKIP, Sif-A and kinesin-interacting

protein; SPAG9, Sperm associated antigen 9; TMEM55B, Transmembrane protein 55B; TRPML1, Mucolipin TRP channel 1; WT, Wild-type

Declarations

Contributions

G.K., M.S. and A.T. conceived and designed the project. G.K. performed the majority of the experiments, analyzed the results, and prepared the figures. P.C. performed the FRB-FKBP based experiments and some lysosome positioning related experiments. S.C., S.S. and K.S. conducted the protein-protein interaction experiments and provided critical molecular biology reagents. M.S. and A.T. wrote the manuscript.

Funding

G.K. and P.C. acknowledge fellowship support from CSIR and IISER Mohali, respectively. This work was supported by the Department of Biotechnology (DBT)/Wellcome Trust India Alliance Intermediate Fellowship (IA/I/14/2/501543) to A.T. and Senior Fellowship (IA/S/19/1/504270) to M.S. The funders had no role in study design, data collection, and interpretation, or the decision to submit the work for publication.

Acknowledgments

The authors acknowledge Prateek Arora (IISER Mohali FACS Facility) for technical help in flow cytometry, Maria Ericson (Harvard Medical School) for help with EM imaging, Ross Tomaino (Taplin MS Facility, Harvard Medical School) for mass spectrometry analysis and Dr. Nitin Mohan (IIT Kanpur) for advice on single-particle tracking related experiments. CSIR-IMTECH Communication No. 016/2021.

Competing interests

The authors declare no competing or financial interests.

References

Abu-Remaileh, M., Wyant, G.A., Kim, C., Laqtom, N.N., Abbasi, M., Chan, S.H., Freinkman, E., and Sabatini, D.M. (2017). Lysosomal metabolomics reveals V-ATPase- and mTOR-dependent regulation of amino acid efflux from lysosomes. Science *358*, 807-813.

Ballabio, A., and Bonifacino, J.S. (2020). Lysosomes as dynamic regulators of cell and organismal homeostasis. Nat Rev Mol Cell Biol *21*, 101-118.

Bonifacino, J.S., and Neefjes, J. (2017). Moving and positioning the endolysosomal system. Curr Opin Cell Biol *47*, 1-8.

Cabukusta, B., and Neefjes, J. (2018). Mechanisms of lysosomal positioning and movement. Traffic *19*, 761-769.

Char, R., and Pierre, P. (2020). The RUFYs, a Family of Effector Proteins Involved in Intracellular Trafficking and Cytoskeleton Dynamics. Front Cell Dev Biol *8*, 779.

Cheng, X.T., Xie, Y.X., Zhou, B., Huang, N., Farfel-Becker, T., and Sheng, Z.H. (2018). Characterization of LAMP1-labeled nondegradative lysosomal and endocytic compartments in neurons. J Cell Biol *217*, 3127-3139.

Choy, C.H., Saffi, G., Gray, M.A., Wallace, C., Dayam, R.M., Ou, Z.A., Lenk, G., Puertollano, R., Watkins, S.C., and Botelho, R.J. (2018). Lysosome enlargement during inhibition of the lipid kinase PIKfyve proceeds through lysosome coalescence. J Cell Sci *131*.

Diwu, Z., Chen, C.S., Zhang, C., Klaubert, D.H., and Haugland, R.P. (1999). A novel acidotropic pH indicator and its potential application in labeling acidic organelles of live cells. Chem Biol *6*, 411-418.

Donaldson, J.G., and Jackson, C.L. (2011). ARF family G proteins and their regulators: roles in membrane transport, development and disease. Nat Rev Mol Cell Biol *12*, 362-375.

Du, W., Su, Q.P., Chen, Y., Zhu, Y., Jiang, D., Rong, Y., Zhang, S., Zhang, Y., Ren, H., Zhang, C.*, et al.* (2016). Kinesin 1 Drives Autolysosome Tubulation. Dev Cell *37*, 326-336.

Dykes, S.S., Gray, A.L., Coleman, D.T., Saxena, M., Stephens, C.A., Carroll, J.L., Pruitt, K., and Cardelli, J.A. (2016). The Arf-like GTPase Arl8b is essential for three-dimensional invasive growth of prostate cancer in vitro and xenograft formation and growth in vivo. Oncotarget *7*, 31037-31052.

Garg, S., Sharma, M., Ung, C., Tuli, A., Barral, D.C., Hava, D.L., Veerapen, N., Besra, G.S., Hacohen, N., and Brenner, M.B. (2011). Lysosomal trafficking, antigen presentation, and microbial killing are controlled by the Arf-like GTPase Arl8b. Immunity *35*, 182-193.

Ghosh, S., Dellibovi-Ragheb, T.A., Kerviel, A., Pak, E., Qiu, Q., Fisher, M., Takvorian, P.M., Bleck, C., Hsu, V.W., Fehr, A.R.*, et al.* (2020). beta-Coronaviruses Use Lysosomes for Egress Instead of the Biosynthetic Secretory Pathway. Cell *183*, 1520-1535 e1514.

Guardia, C.M., Farias, G.G., Jia, R., Pu, J., and Bonifacino, J.S. (2016). BORC Functions Upstream of Kinesins 1 and 3 to Coordinate Regional Movement of Lysosomes along Different Microtubule Tracks. Cell Rep *17*, 1950-1961.

Guha, S., Coffey, E.E., Lu, W., Lim, J.C., Beckel, J.M., Laties, A.M., Boesze-Battaglia, K., and Mitchell, C.H. (2014). Approaches for detecting lysosomal alkalinization and impaired degradation in fresh and cultured RPE cells: evidence for a role in retinal degenerations. Exp Eye Res *126*, 68-76.

Hofmann, I., and Munro, S. (2006). An N-terminally acetylated Arf-like GTPase is localised to lysosomes and affects their motility. J Cell Sci *119*, 1494-1503.

Homma, Y., Hiragi, S., and Fukuda, M. (2021). Rab family of small GTPases: an updated view on their regulation and functions. FEBS J *288*, 36-55.

Honda, A., Usui, H., Sakimura, K., and Igarashi, M. (2017). Rufy3 is an adapter protein for small GTPases that activates a Rac guanine nucleotide exchange factor to control neuronal polarity. J Biol Chem *292*, 20936-20946.

Hunt, S.D., and Stephens, D.J. (2011). The role of motor proteins in endosomal sorting. Biochem Soc Trans *39*, 1179-1184.

Jia, R., and Bonifacino, J.S. (2019). Lysosome Positioning Influences mTORC2 and AKT Signaling. Mol Cell *75*, 26-38 e23.

Jia, R., Guardia, C.M., Pu, J., Chen, Y., and Bonifacino, J.S. (2017). BORC coordinates encounter and fusion of lysosomes with autophagosomes. Autophagy *13*, 1648-1663.

Johansson, M., Rocha, N., Zwart, W., Jordens, I., Janssen, L., Kuijl, C., Olkkonen, V.M., and Neefjes, J. (2007). Activation of endosomal dynein motors by stepwise assembly of Rab7-RILP-p150Glued, ORP1L, and the receptor betalll spectrin. J Cell Biol *176*, 459-471.

Johnson, D.E., Ostrowski, P., Jaumouille, V., and Grinstein, S. (2016). The position of lysosomes within the cell determines their luminal pH. J Cell Biol *212*, 677-692.

Johnston, J.A., Illing, M.E., and Kopito, R.R. (2002). Cytoplasmic dynein/dynactin mediates the assembly of aggresomes. Cell Motil Cytoskeleton *53*, 26-38.

Jongsma, M.L., Berlin, I., Wijdeven, R.H., Janssen, L., Janssen, G.M., Garstka, M.A., Janssen, H., Mensink, M., van Veelen, P.A., Spaapen, R.M.*, et al.* (2016). An ER-Associated Pathway Defines Endosomal Architecture for Controlled Cargo Transport. Cell *166*, 152-166.

Jordens, I., Fernandez-Borja, M., Marsman, M., Dusseljee, S., Janssen, L., Calafat, J., Janssen, H., Wubbolts, R., and Neefjes, J. (2001). The Rab7 effector protein RILP controls lysosomal transport by inducing the recruitment of dynein-dynactin motors. Curr Biol *11*, 1680-1685.

Keren-Kaplan, T., and Bonifacino, J.S. (2021). ARL8 Relieves SKIP Autoinhibition to Enable Coupling of Lysosomes to Kinesin-1. Curr Biol *31*, 540-554 e545.

Kesisova, I.A., Robinson, B.P., and Spiliotis, E.T. (2021). A septin GTPase scaffold of dynein-dynactin motors triggers retrograde lysosome transport. J Cell Biol *220*.

Khatter, D., Raina, V.B., Dwivedi, D., Sindhwani, A., Bahl, S., and Sharma, M. (2015a). The small GTPase Arl8b regulates assembly of the mammalian HOPS complex on lysosomes. J Cell Sci *128*, 1746-1761.

Khatter, D., Sindhwani, A., and Sharma, M. (2015b). Arf-like GTPase Arl8: Moving from the periphery to the center of lysosomal biology. Cell Logist *5*, e1086501.

Kimura, S., Noda, T., and Yoshimori, T. (2008). Dynein-dependent movement of autophagosomes mediates efficient encounters with lysosomes. Cell Struct Funct *33*, 109-122.

Kitagishi, Y., and Matsuda, S. (2013). RUFY, Rab and Rap Family Proteins Involved in a Regulation of Cell Polarity and Membrane Trafficking. Int J Mol Sci *14*, 6487-6498.

Kjos, I., Vestre, K., Guadagno, N.A., Borg Distefano, M., and Progida, C. (2018). Rab and Arf proteins at the crossroad between membrane transport and cytoskeleton dynamics. Biochim Biophys Acta Mol Cell Res *1865*, 1397-1409.

Klionsky, D.J., Abdel-Aziz, A.K., Abdelfatah, S., Abdellatif, M., Abdoli, A., Abel, S., Abeliovich, H., Abildgaard, M.H., Abudu, Y.P., Acevedo-Arozena, A.*, et al.* (2021). Guidelines for the use and interpretation of assays for monitoring autophagy (4th edition). Autophagy, 1-382.

Korolchuk, V.I., Saiki, S., Lichtenberg, M., Siddiqi, F.H., Roberts, E.A., Imarisio, S., Jahreiss, L., Sarkar, S., Futter, M., Menzies, F.M.*, et al.* (2011). Lysosomal positioning coordinates cellular nutrient responses. Nat Cell Biol *13*, 453-460.

Laopanupong, T., Prombutara, P., Kanjanasirirat, P., Benjaskulluecha, S., Boonmee, A., Palaga, T., Meresse, S., Paha, J., Siregar, T.A.P., Khumpanied, T.*, et al.* (2021). Lysosome repositioning as an autophagy escape mechanism by Mycobacterium tuberculosis Beijing strain. Sci Rep *11*, 4342.

Li, X., Rydzewski, N., Hider, A., Zhang, X., Yang, J., Wang, W., Gao, Q., Cheng, X., and Xu, H. (2016). A molecular mechanism to regulate lysosome motility for lysosome positioning and tubulation. Nat Cell Biol *18*, 404-417.

Lu, M., van Tartwijk, F.W., Lin, J.Q., Nijenhuis, W., Parutto, P., Fantham, M., Christensen, C.N., Avezov, E., Holt, C.E., Tunnacliffe, A.*, et al.* (2020). The structure and global distribution of the endoplasmic reticulum network are actively regulated by lysosomes. Sci Adv *6*.

Ma, L., Ouyang, Q., Werthmann, G.C., Thompson, H.M., and Morrow, E.M. (2017). Live-cell Microscopy and Fluorescence-based Measurement of Luminal pH in Intracellular Organelles. Front Cell Dev Biol *5*, 71.

Marwaha, R., Arya, S.B., Jagga, D., Kaur, H., Tuli, A., and Sharma, M. (2017). The Rab7 effector PLEKHM1 binds Arl8b to promote cargo traffic to lysosomes. J Cell Biol *216*, 1051-1070.

Michelet, X., Tuli, A., Gan, H., Geadas, C., Sharma, M., Remold, H.G., and Brenner, M.B. (2018). Lysosome-Mediated Plasma Membrane Repair Is Dependent on the Small GTPase Arl8b and Determines Cell Death

Type in Mycobacterium tuberculosis Infection. J Immunol *200*, 3160-3169.

Mori, T., Wada, T., Suzuki, T., Kubota, Y., and Inagaki, N. (2007). Singar1, a novel RUN domain-containing protein, suppresses formation of surplus axons for neuronal polarity. J Biol Chem *282*, 19884-19893.

Mrakovic, A., Kay, J.G., Furuya, W., Brumell, J.H., and Botelho, R.J. (2012). Rab7 and Arl8 GTPases are necessary for lysosome tubulation in macrophages. Traffic *13*, 1667-1679.

Pankiv, S., Alemu, E.A., Brech, A., Bruun, J.A., Lamark, T., Overvatn, A., Bjorkoy, G., and Johansen, T. (2010). FYCO1 is a Rab7 effector that binds to LC3 and PI3P to mediate microtubule plus end-directed vesicle transport. J Cell Biol *188*, 253-269.

Ponsford, A.H., Ryan, T.A., Raimondi, A., Cocucci, E., Wycislo, S.A., Frohlich, F., Swan, L.E., and Stagi, M. (2020). Live imaging of intra-lysosome pH in cell lines and primary neuronal culture using a novel genetically encoded biosensor. Autophagy, 1-19.

Pu, J., Keren-Kaplan, T., and Bonifacino, J.S. (2017). A Ragulator-BORC interaction controls lysosome positioning in response to amino acid availability. J Cell Biol *216*, 4183-4197.

Pu, J., Schindler, C., Jia, R., Jarnik, M., Backlund, P., and Bonifacino, J.S. (2015). BORC, a multisubunit complex that regulates lysosome positioning. Dev Cell *33*, 176-188.

Rabanal-Ruiz, Y., Byron, A., Wirth, A., Madsen, R., Sedlackova, L., Hewitt, G., Nelson, G., Stingele, J., Wills, J.C., Zhang, T.*, et al.* (2021). mTORC1 activity is supported by spatial association with focal adhesions. J Cell Biol *220*.

Reck-Peterson, S.L., Redwine, W.B., Vale, R.D., and Carter, A.P. (2018). The cytoplasmic dynein transport machinery and its many cargoes. Nat Rev Mol Cell Biol *19*, 382-398.

Rishal, I., Kam, N., Perry, R.B., Shinder, V., Fisher, E.M., Schiavo, G., and Fainzilber, M. (2012). A motor-driven mechanism for cell-length sensing. Cell Rep *1*, 608-616.

Rosa-Ferreira, C., and Munro, S. (2011). Arl8 and SKIP act together to link lysosomes to kinesin-1. Dev Cell *21*, 1171-1178.

Saffi, G.T., and Botelho, R.J. (2019). Lysosome Fission: Planning for an Exit. Trends Cell Biol *29*, 635-646.

Saric, A., Hipolito, V.E., Kay, J.G., Canton, J., Antonescu, C.N., and Botelho, R.J. (2016). mTOR controls lysosome tubulation and antigen presentation in macrophages and dendritic cells. Mol Biol Cell *27*, 321-333.

Schiefermeier, N., Scheffler, J.M., de Araujo, M.E., Stasyk, T., Yordanov, T., Ebner, H.L., Offterdinger, M., Munck, S., Hess, M.W., Wickstrom, S.A.*, et al.* (2014). The late endosomal p14-MP1 (LAMTOR2/3) complex regulates focal adhesion dynamics during cell migration. J Cell Biol *205*, 525-540.

Schindelin, J., Arganda-Carreras, I., Frise, E., Kaynig, V., Longair, M., Pietzsch, T., Preibisch, S., Rueden, C., Saalfeld, S., Schmid, B.*, et al.* (2012). Fiji: an open-source platform for biological-image analysis. Nat Methods *9*, 676-682.

Sharma, G., Guardia, C.M., Roy, A., Vassilev, A., Saric, A., Griner, L.N., Marugan, J., Ferrer, M., Bonifacino, J.S., and DePamphilis, M.L. (2019). A family of PIKFYVE inhibitors with therapeutic potential against autophagy-dependent cancer cells disrupt multiple events in lysosome homeostasis. Autophagy *15*, 1694-1718.

Sindhwani, A., Arya, S.B., Kaur, H., Jagga, D., Tuli, A., and Sharma, M. (2017). Salmonella exploits the host endolysosomal tethering factor HOPS complex to promote its intravacuolar replication. PLoS Pathog *13*, e1006700.

Soppina, V., Rai, A.K., Ramaiya, A.J., Barak, P., and Mallik, R. (2009). Tug-of-war between dissimilar teams of microtubule motors regulates transport and fission of endosomes. Proc Natl Acad Sci U S A *106*, 19381-19386.

Spits, M., Heesterbeek, I.T., Voortman, L.M., Akkermans, J.J., Wijdeven, R.H., Cabukusta, B., and Neefjes, J. (2021). Mobile late endosomes modulate peripheral endoplasmic reticulum network architecture. EMBO Rep, e50815.

Takemasu, S., Nigorikawa, K., Yamada, M., Tsurumi, G., Kofuji, S., Takasuga, S., and Hazeki, K. (2019). Phosphorylation of TMEM55B by Erk/MAPK regulates lysosomal positioning. J Biochem *166*, 175-185.

Tinevez, J.Y., Perry, N., Schindelin, J., Hoopes, G.M., Reynolds, G.D., Laplantine, E., Bednarek, S.Y., Shorte, S.L., and Eliceiri, K.W. (2017). TrackMate: An open and extensible platform for single-particle tracking. Methods *115*, 80-90.

Tuli, A., and Sharma, M. (2019). How to do business with lysosomes: Salmonella leads the way. Curr Opin Microbiol *47*, 1-7.

Tuli, A., Thiery, J., James, A.M., Michelet, X., Sharma, M., Garg, S., Sanborn, K.B., Orange, J.S., Lieberman, J., and Brenner, M.B. (2013). Arf-like GTPase Arl8b regulates lytic granule polarization and natural killer cell-mediated cytotoxicity. Mol Biol Cell *24*, 3721-3735.

Vogel, G.F., Ebner, H.L., de Araujo, M.E., Schmiedinger, T., Eiter, O., Pircher, H., Gutleben, K., Witting, B., Teis, D., Huber, L.A.*, et al.* (2015). Ultrastructural Morphometry Points to a New Role for LAMTOR2 in Regulating the Endo/Lysosomal System. Traffic *16*, 617-634.

Wang, G., Zhang, Q., Song, Y., Wang, X., Guo, Q., Zhang, J., Li, J., Han, Y., Miao, Z., and Li, F. (2015). PAK1 regulates RUFY3-mediated gastric cancer cell migration and invasion. Cell Death Dis *6*, e1682.

Wei, Z., Sun, M., Liu, X., Zhang, J., and Jin, Y. (2014). Rufy3, a protein specifically expressed in neurons, interacts with actin-bundling protein Fascin to control the growth of axons. J Neurochem *130*, 678-692.

Willett, R., Martina, J.A., Zewe, J.P., Wills, R., Hammond, G.R.V., and Puertollano, R. (2017). TFEB regulates lysosomal positioning by modulating TMEM55B expression and JIP4 recruitment to lysosomes. Nat Commun *8*, 1580.

Xie, R., Wang, J., Tang, W., Li, Y., Peng, Y., Zhang, H., Liu, G., Huang, X., Zhao, J., Li, A.*, et al.* (2017). Rufy3 promotes metastasis through epithelial-mesenchymal transition in colorectal cancer. Cancer Lett *390*, 30-38.

Yordanov, T.E., Hipolito, V.E.B., Liebscher, G., Vogel, G.F., Stasyk, T., Herrmann, C., Geley, S., Teis, D., Botelho, R.J., Hess, M.W.*, et al.* (2019). Biogenesis of lysosome-related organelles complex-1 (BORC) regulates late endosomal/lysosomal size through PIKfyve-dependent phosphatidylinositol-3,5-bisphosphate. Traffic *20*, 674-696.

Figures

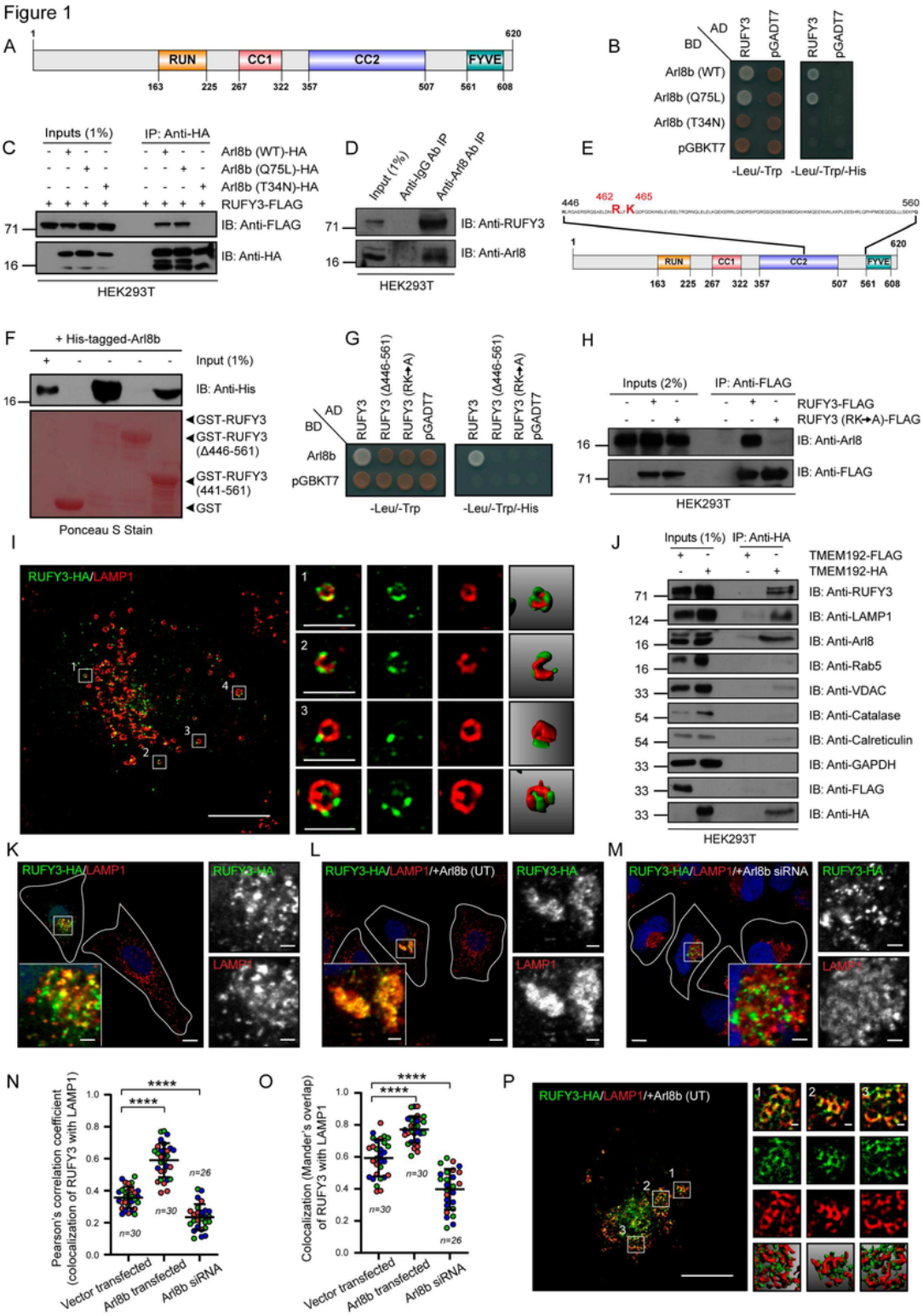

Figure 1

Arl8b directly binds and recruit RUFY3 on lysosomes. (A) Schematic representation of the domain architecture of RUFY3 protein. Domain predictions show an N-terminal RUN domain, two CC (coiled-coil) domain and a C-terminal FYVE-like domain (numbers are amino acid positions). (B) Plasmid encoding GAL4-AD fused to RUFY3 was co-transformed with Arl8b-WT (Wild-type), -Q75L (GTP-bound) and -T34N (GDP-bound) forms fused to GAL4-BD in S. cerevisiae to examine the interactions. The co-transformants

were spotted on non-selective medium (-Leu/-Trp) to confirm viability and selective medium (-Leu/-Trp/-His) to detect interactions. (C) A plasmid expressing RUFY3-FLAG-tagged was co-transfected with different forms of C-terminal HA-tagged Arl8b into HEK293T cells, lysates were immunoprecipitated (IP) with anti-HA antibodies-conjugated-agarose beads. The precipitates were immunoblotted (IB) with the indicated antibodies. (D) Endogenous IP was performed by incubating the HEK293T cell lysates with mouse anti-Arl8 antibody-conjugated-resin or mouse IgG-conjugated-resin (as a control), and precipitates were IB with indicated antibodies. (E) Schematic representation of Arl8b-binding region of RUFY3 indicating the amino acid residues (R462 and K465) important for binding to Arl8b. (F) Recombinant GST alone, GST-RUFY3 (WT), GST-RUFY3 (Δ446-561 aa) and GST-RUFY3 (441-561 aa) proteins were immobilized on glutathione conjugated-agarose beads and incubated with purified His-Arl8b. The interaction of the purified proteins was detected by Western blotting. Ponceau S staining of the blot was done to visualize purified proteins. (G) The binding of point mutants of RUFY3 (R462A/K465A; RK→A) with Arl8b was tested using the yeast two-hybrid system. The co-transformants were spotted on non-selective medium (-Leu/-Trp) for checking viability and selective medium (-Leu/-Trp/-His) for testing interactions. (H) Lysates of HEK293T cells expressing RUFY3-FLAG or RUFY3 (RK→A)-FLAG was IP with anti-FLAG antibodies-conjugated-agarose beads, and the precipitates were IB with the indicated antibodies. (I) Representative SIM image of a HeLa cell transfected with RUFY3-HA construct and stained for lysosomes using an anti-LAMP1 antibody. Before fixation, cytosol was leached to visualize the RUFY3 signal better. Insets show magnification of selected vesicles, highlighting the presence of RUFY3 on the LAMP1-positive vesicles. The fourth column of insets shows an isosurface view of vesicles generated using Imaris software. Scale Bars: (main) 10 μm; (insets) 2 μm. (J) RUFY3, similar to LAMP1 and Arl8b, was present in the lysosomal fractions under endogenous conditions. Lysates were prepared from HEK293T cells expressing TMEM192-FLAG (control) or TMEM192-HA and subjected to lysosome purification using the LysoIP method. The isolated fractions were IB for protein markers of various subcellular compartments. (K-M) RUFY3 lysosomal localization requires Arl8b. Representative confocal micrographs of cytosol-leached HeLa cells transfected with RUFY3-HA construct (K), co-transfected with RUFY3-HA and Arl8b untagged (UT) constructs (L) and Arl8b siRNA treated and transfected with RUFY3-HA construct (M), and stained for lysosomes using an anti-LAMP1 antibody. RUFY3 localization to LAMP1-positive compartments is shown in insets. Scale Bars: (main) 10 μm; (insets) 2 μm. (N-O) Colocalization of RUFY3-HA with LAMP1-positive compartments for experiments presented in (K-M) was quantified using Pearson's correlation coefficient (N) and Mander's overlap (O). Values plotted are mean ± S.D. from three independent experiments. Experiments are color-coded, and each dot represents the individual data points from each experiment. The total number of cells analyzed is indicated on the top or bottom of each data set (****$p<0.0001$; Student's t-test). (P) Representative SIM micrograph of cytosol-leached HeLa cells co-transfected with RUFY3-HA and Arl8b (UT) constructs. The insets depict enhanced colocalization of RUFY3 on lysosomes in the presence of Arl8b. Scale Bars: (main) 10 μm; (insets) 2 μm.

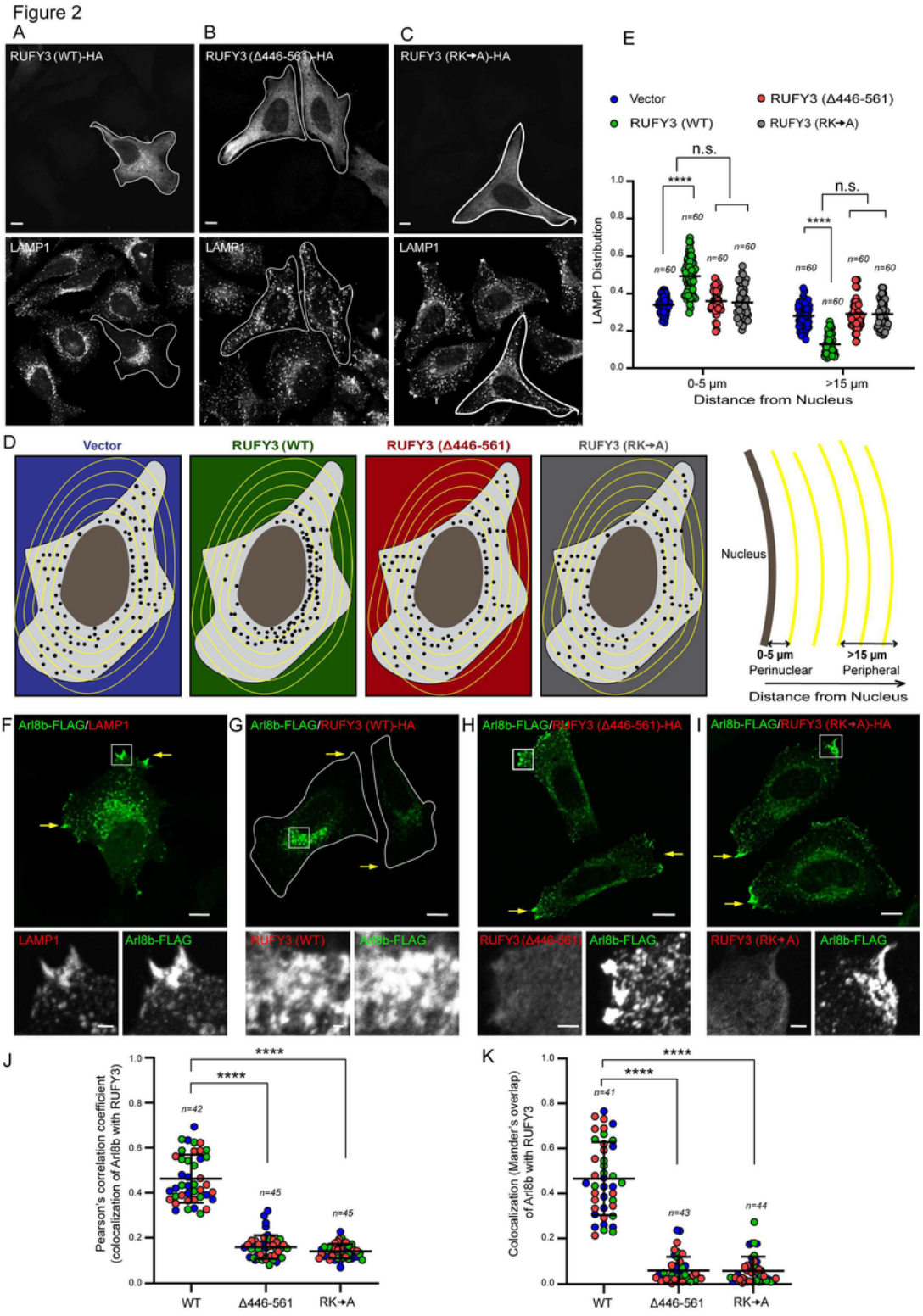

Figure 2

Wild-type RUFY3, but not the Arl8b binding-defective mutant, promotes perinuclear lysosome clustering. (A-C) Representative confocal micrographs of HeLa cells expressing RUFY3-HA (WT) (A), RUFY3 (Δ446-561)-HA (B) and RUFY3 (RK→A)-HA (C) and stained for lysosomes using an anti-LAMP1 antibody. Scale Bars: (main) 10 μm; (insets) 2 μm. (D) A schematic depicting the quantification method employed for analyzing the distribution of LAMP1-positive compartments in a cell. (E) The distribution of LAMP1-

positive compartments in HeLa cell transfected with indicated plasmids was measured as shown in (D). Values plotted are mean ± S.D. from three independent experiments. The total number of cells analyzed is indicated on top of each data set (****p<0.0001; n.s., not significant; Student's t-test). (F-I) Representative confocal micrographs of HeLa cells transfected with Arl8b-FLAG alone (F) or co-transfected with Arl8b-FLAG and indicated RUFY3 expressing plasmids and stained for indicated antibodies. Yellow arrows mark the peripheral localization of Arl8b-positive vesicles. Scale Bars: (main) 10 μm; (insets) 2 μm. (J-K) Colocalization analysis of Arl8b with indicated RUFY3 proteins was assessed by calculating Pearson's correlation coefficient (J) and Mander's overlap (K). Values plotted are mean ± S.D. from three independent experiments. Experiments are color-coded, and each dot represents the individual data points from each experiment. The total number of cells analyzed is indicated on top of each data set (****p<0.0001; Student's t-test).

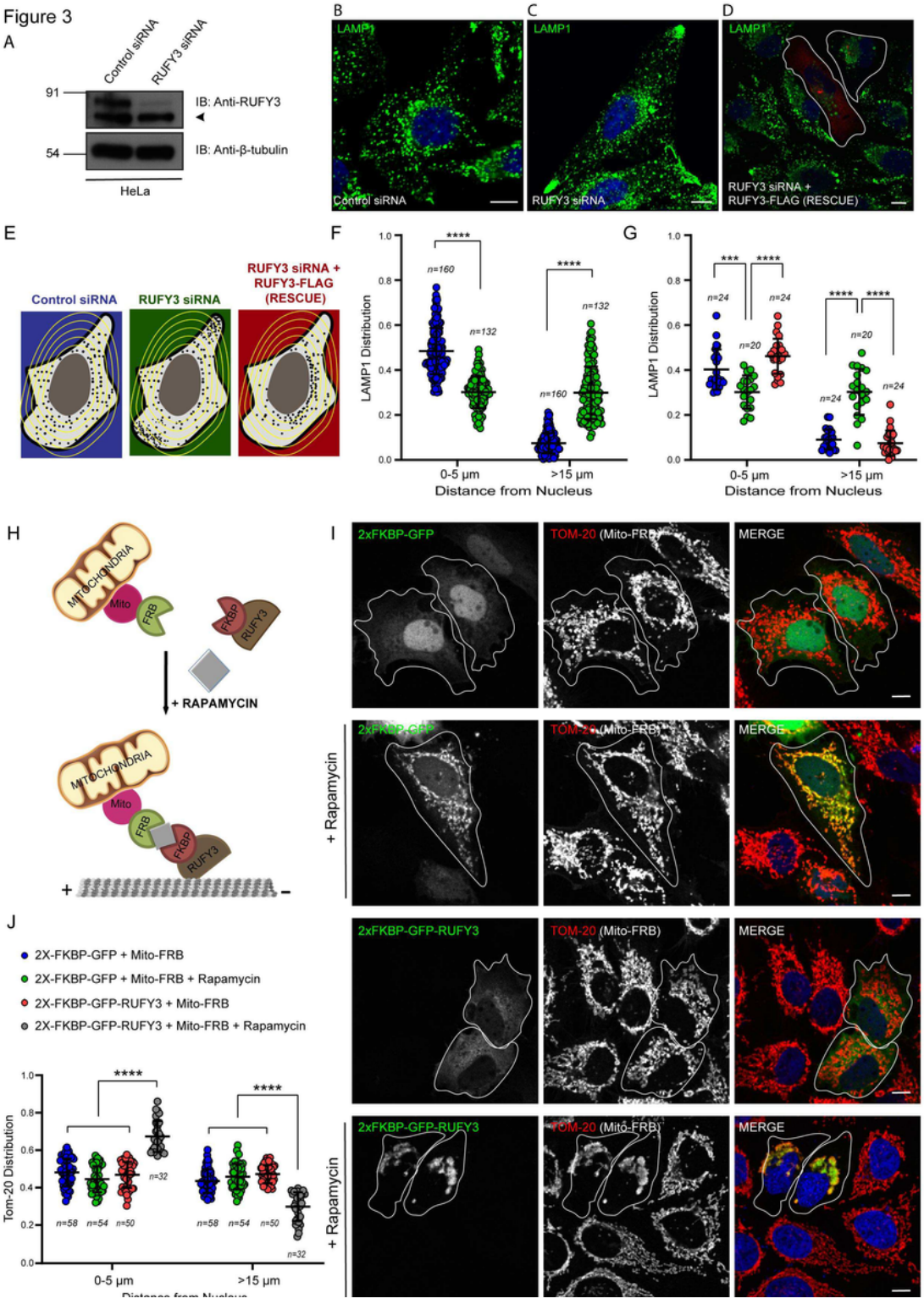

Figure 3

RUFY3 is essential and sufficient to drive perinuclear lysosome positioning. (A) The efficiency of RUFY3 silencing in HeLa cells. Lysates of HeLa cells treated with control- and RUFY3-siRNA were IB using the anti-RUFY3 antibody. The arrowhead corresponds to a non-specific signal detected by the antibody. The blot was also probed for β-tubulin for the equal amount of protein loading. (B-D) Representative confocal micrographs showing lysosome distribution in HeLa cells treated with indicated siRNAs. The lysosomes

were stained using an anti-LAMP1 antibody, and a white boundary outlines the cell showing expression of RUFY3 siRNA-rescue construct. Scale Bar: 10 μm. (E) Cartoon depicting the effect on the distribution of lysosomes in cells upon treatment with indicated siRNAs. (F-G) The distribution of LAMP1-positive lysosomes was quantified from the experiments presented in (B-D). Values plotted are mean ± S.D. from three independent experiments. The total number of cells analyzed is indicated on top of each data set (****p<0.0001; ***p<0.001; Student's t-test). (H) Schematic representation of the rapamycin-inducible FRB/FKBP protein-protein interaction. (I) Representative confocal micrographs of untreated- and rapamycin treated-HeLa cells expressing Mito-FRB with 2xFKBP-GFP or 2xFKBP-GFP-RUFY3. To visualize mitochondria, cells were stained using an anti-TOM-20 antibody. Scale Bar: 10 μm. (J) The distribution of mitochondria based on the Tom-20 signal was quantified from the images shown in (I). Values plotted are mean ± S.D. from three independent experiments. The total number of cells analyzed is indicated below each data set (****p<0.0001; Student's t-test).

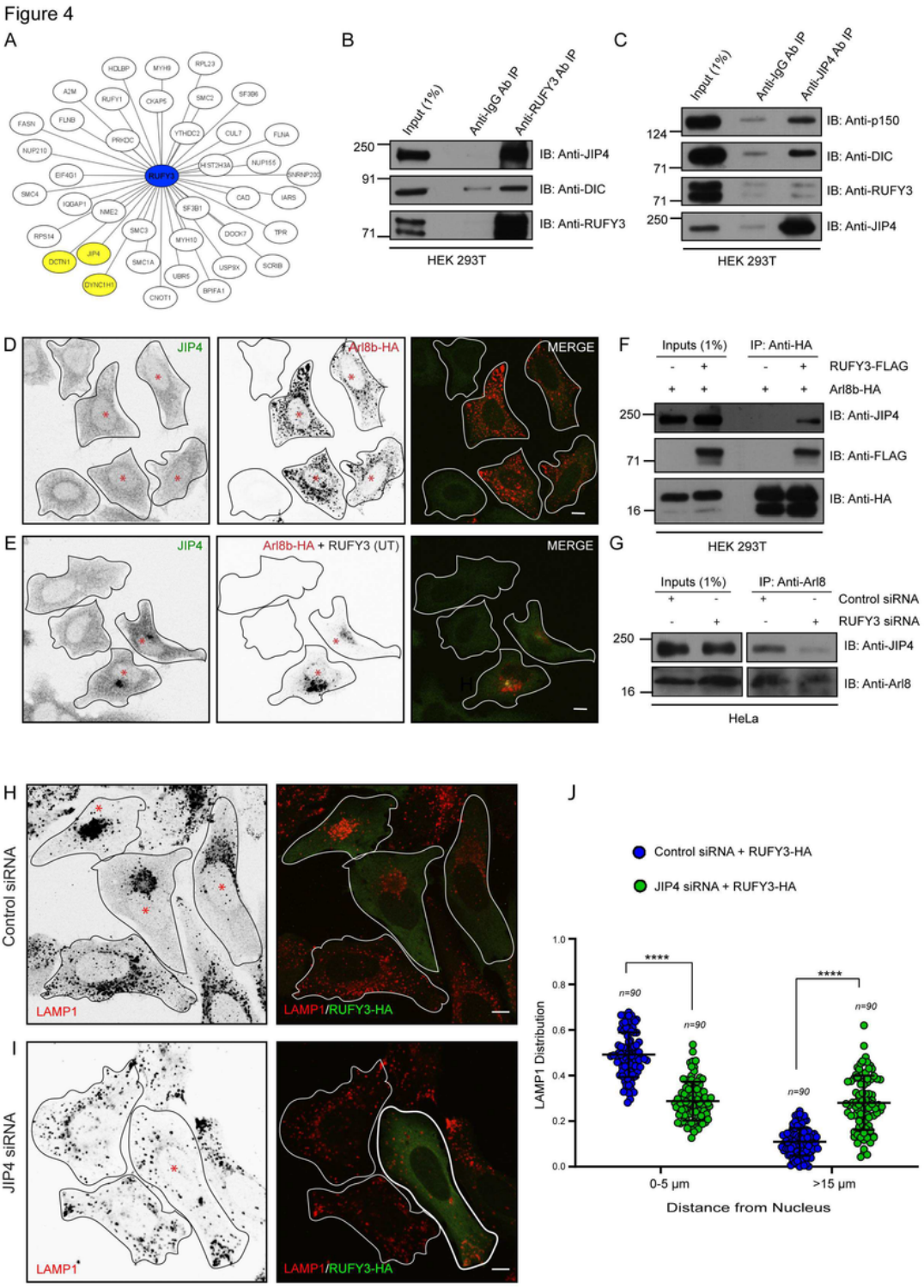

Figure 4

RUFY3 links Arl8b to the JIP4-dynein complex. (A) Network representation of RUFY3 (shown in blue circle) and its associated proteins constructed by using Cytoscape. For clarity, only a subset of identified proteins with greater than five-fold enrichment in GST-RUFY3 eluate compared to GST only is shown. Association of RUFY3 with cytoplasmic dynein heavy chain (DYNC1H1/DHC), dynactin 1/p150glued (DCTN1) and C-Jun-amino-terminal kinase-interacting protein 4 (JIP4) is shown in yellow circles. (B-C)

Lysates of HEK293T cells were subjected to IP using antibodies against RUFY3, JIP4 and isotype control, and the precipitates were IB with indicated antibodies. (D-E) Representative confocal micrographs of HeLa cells transfected with Arl8b-HA construct (D) or co-transfected with Arl8b-HA and RUFY3 (UT) constructs (E) and stained with indicated antibodies. An asterisk marks the transfected cells, and some panels are shown in an inverted grayscale for better visualization. Scale Bars: 10 μm. (F) Lysates of HEK293T cells expressing Arl8b-HA or co-expressing Arl8b-HA and RUFY3-FLAG were lysed and subjected to IP using anti-HA antibodies-conjugated-agarose beads and the precipitates were IB with the indicated antibodies. (G) HeLa cells were treated with control siRNA or RUFY3 siRNA and subjected to endogenous IP using an anti-Arl8 antibody. The precipitates were IB with indicated antibodies. (H-I) Representative confocal images of HeLa cells treated with control siRNA (H) or JIP4 siRNA (I) and transfected with RUFY3-HA expressing construct. The cells were stained for lysosomes and RUFY3 using anti-LAMP1 and anti-HA antibodies, respectively. An asterisk marks the transfected cells, and some panels are shown in an inverted grayscale for better visualization. Scale Bars: 10 μm. (J) The distribution of lysosomes based on the LAMP1 signal was quantified from the images shown in (H-I). Values plotted are mean ± S.D. from three independent experiments. The total number of cells analyzed is indicated above each data set (****$p<0.0001$; Student’s t-test).

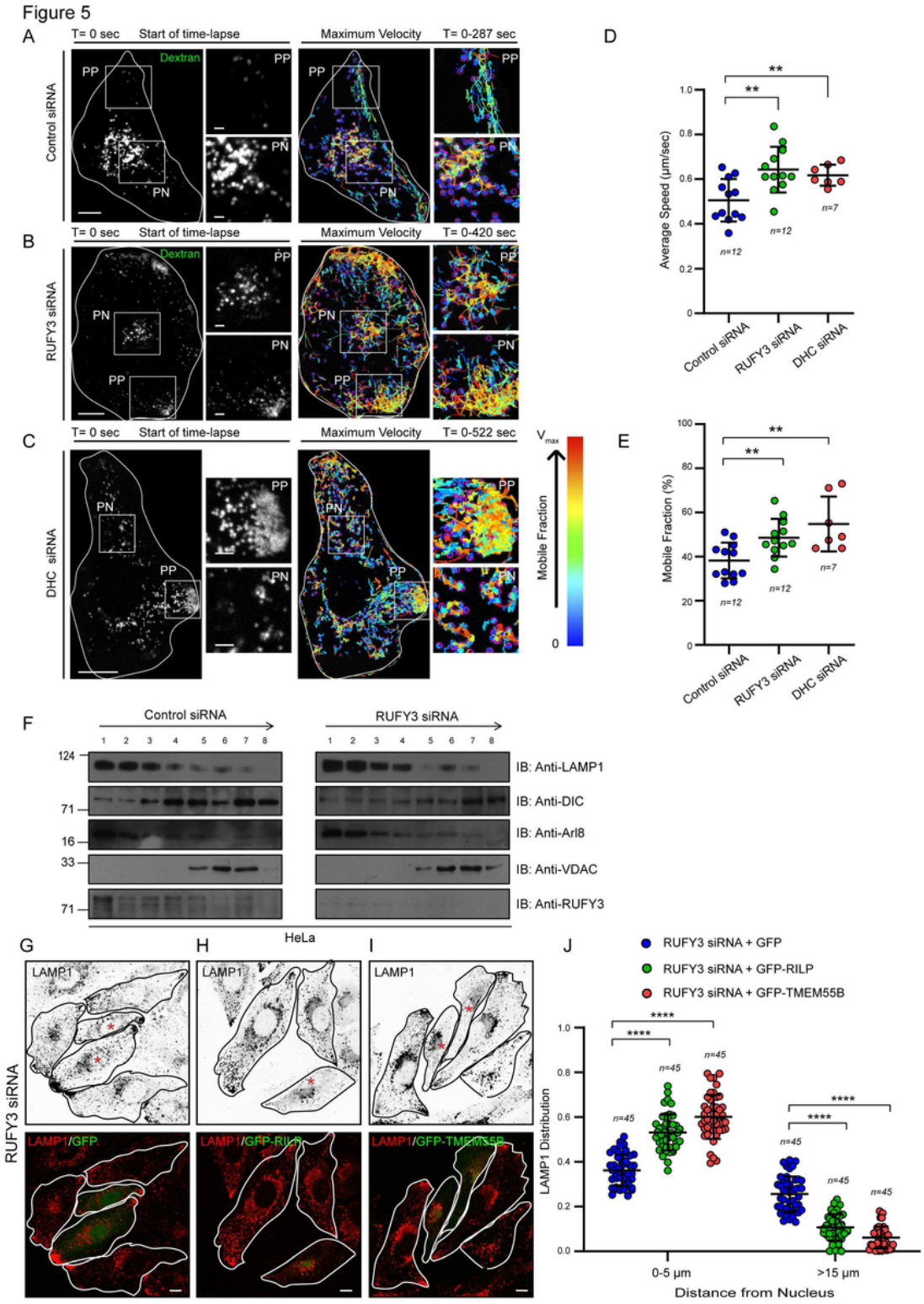

Figure 5

RUFY3 mediates lysosome motility by recruiting dynein motor on lysosomes. (A-C) HeLa cells treated with control siRNA (A), RUFY3 siRNA (B) or DHC siRNA (C) were pre-incubated with Alexa-Fluor 488-conjugated dextran (12 hr pulse and 8 hr chase) to label lysosomes. Left panels: representative confocal images of live HeLa cells captured at the start of time-lapse imaging (T=0 sec). Right panels: single-particle tracking analysis of dextran-labeled lysosomes for designated time-period with color-coding to

show maximum velocity (blue, immobile; red, max mobility). Insets highlights boxed peripheral (PP) and perinuclear (PN) regions of the cell. Scale Bars: (main) 10 μm; (insets) 2 μm; see Supplementary Movies: S1-3. (D-E) The graph represents maximum average speed (D) and a mobile fraction (E) of dextran-labeled lysosomes calculated from two independent live-cell imaging experiments as described in (A-C). Values plotted are mean ± S.D., and the total number of cells analyzed is shown below each data set (**p<0.01; Student's t-test). (F) Lysosomes enrichment was performed using Opti-prep density ultracentrifugation on post-nuclear homogenate prepared from HeLa cells treated with control siRNA or RUFY3 siRNA. Different fractions were resolved and IB using indicated antibodies. (G-I) Representative confocal images of RUFY3-siRNA treated HeLa cells transfected with GFP (G), GFP-RILP (H) or GFP-TMEM55B (I) and stained for lysosomes using an anti-LAMP1 antibody. An asterisk marks the transfected cells, and some panels are shown in an inverted grayscale for better visualization. Scale Bars: 10 μm. (J) The distribution of lysosomes based on the LAMP1 signal was quantified from the images shown in (G-I). Values plotted are mean ± S.D. from three independent experiments. The total number of cells analyzed is indicated above each data set (****p<0.0001; Student's t-test).

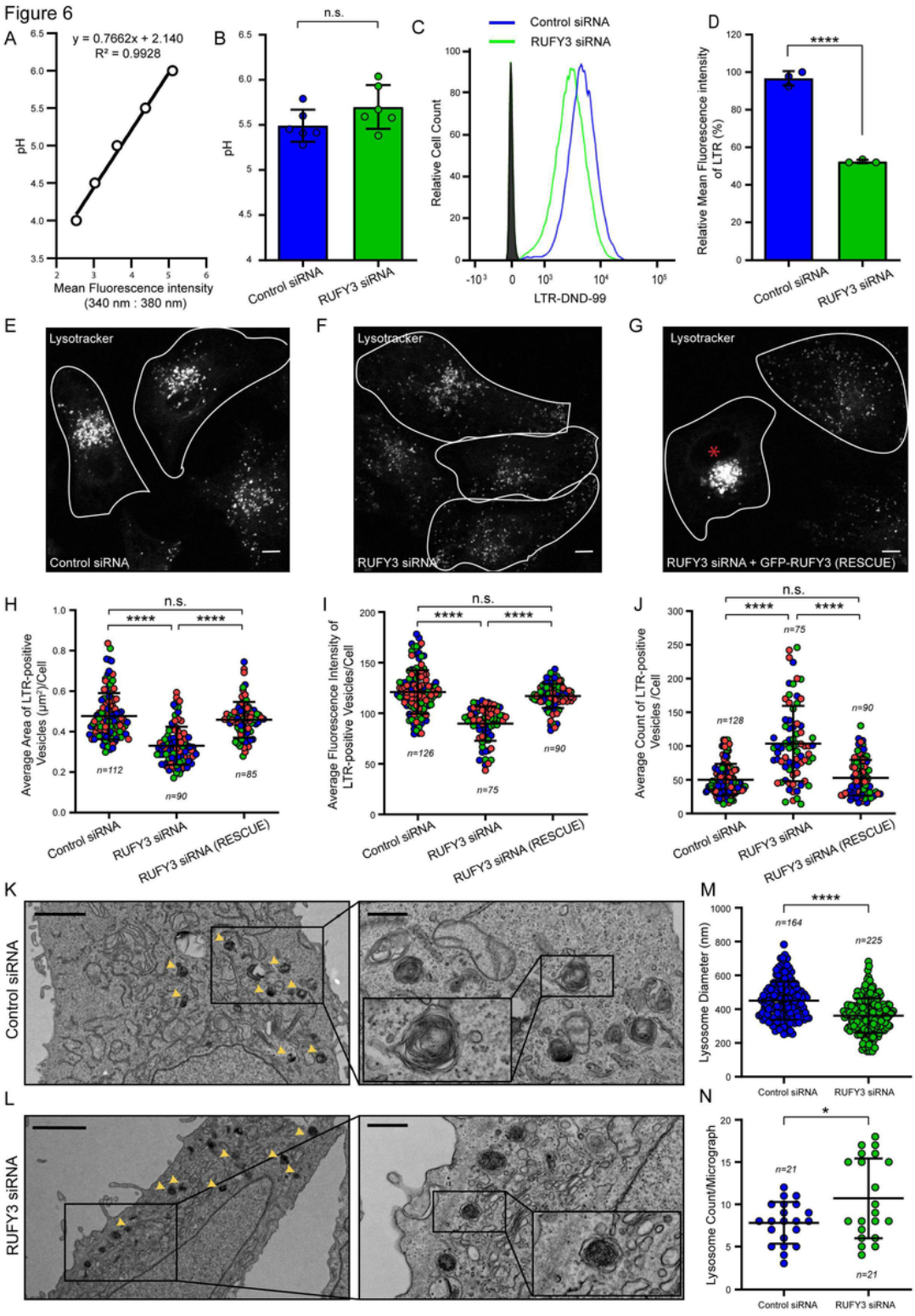

Figure 6

RUFY3 depletion reduces lysosome size. (A) Representative pH calibration curve graph generated based on ratiometric fluorescence intensity measurements of LysoSensorTM Yellow/Blue DND-160 in HeLa cells incubated with different pH calibration buffers. (B) Graph showing average pH-value of lysosomes measured from control siRNA- and RUFY3 siRNA-treated HeLa cells. Values plotted are mean ± S.D. from six independent experiments (n.s., not significant; Student's t-test). (C-D) Representative histogram

showing mean fluorescence intensity (MFI) of Lysotracker Red DND-99 uptake (1 hr) in control siRNA- and RUFY3 siRNA-treated HeLa cells as analyzed by flow cytometry (C), and the bar graph in (D) represents relative percentage of MFI signal for Lysotracker DND-99 uptake (1 hr) in HeLa cells treated with control- or RUFY3-siRNA calculated from three independent experiments (****p<0.0001; Student's t-test). (E-G) Representative confocal micrographs of live HeLa cells treated with indicated siRNAs and incubated with lysotracker (LTR DND-99). The asterisk in (G) marks cell transfected with GFP-RUFY3-siRNA-resistant expressing plasmid. Scale Bars: 10 μm. (H-J) Quantification of average area (H), average fluorescence intensity (I) and average count (J) of LTR-positive vesicles in HeLa cells transfected with indicated siRNAs. Values plotted are mean ± S.D. from three independent experiments. Experiments are color-coded, and each dot represents the individual data points from each experiment. The total number of cells analyzed is indicated on the top or bottom of each data set (n.s., not significant; ****p<0.0001; Student's t-test). (K-N) Representative TEM images of control siRNA (K)-and RUFY3 siRNA (L)-treated HeLa cells. Higher magnifications of lysosomes (dense and multi-lamellar structures, indicated by yellow arrowheads) are shown in the right panels. Scale Bars: 2 μm (main); 0.5 μm (inset). Lysosomes size (M) and numbers (N) were quantified using TEM images of HeLa cells treated with indicated siRNAs. Values plotted are mean ± S.D. (*p<0.05; ****p<0.0001; Student's t-test).

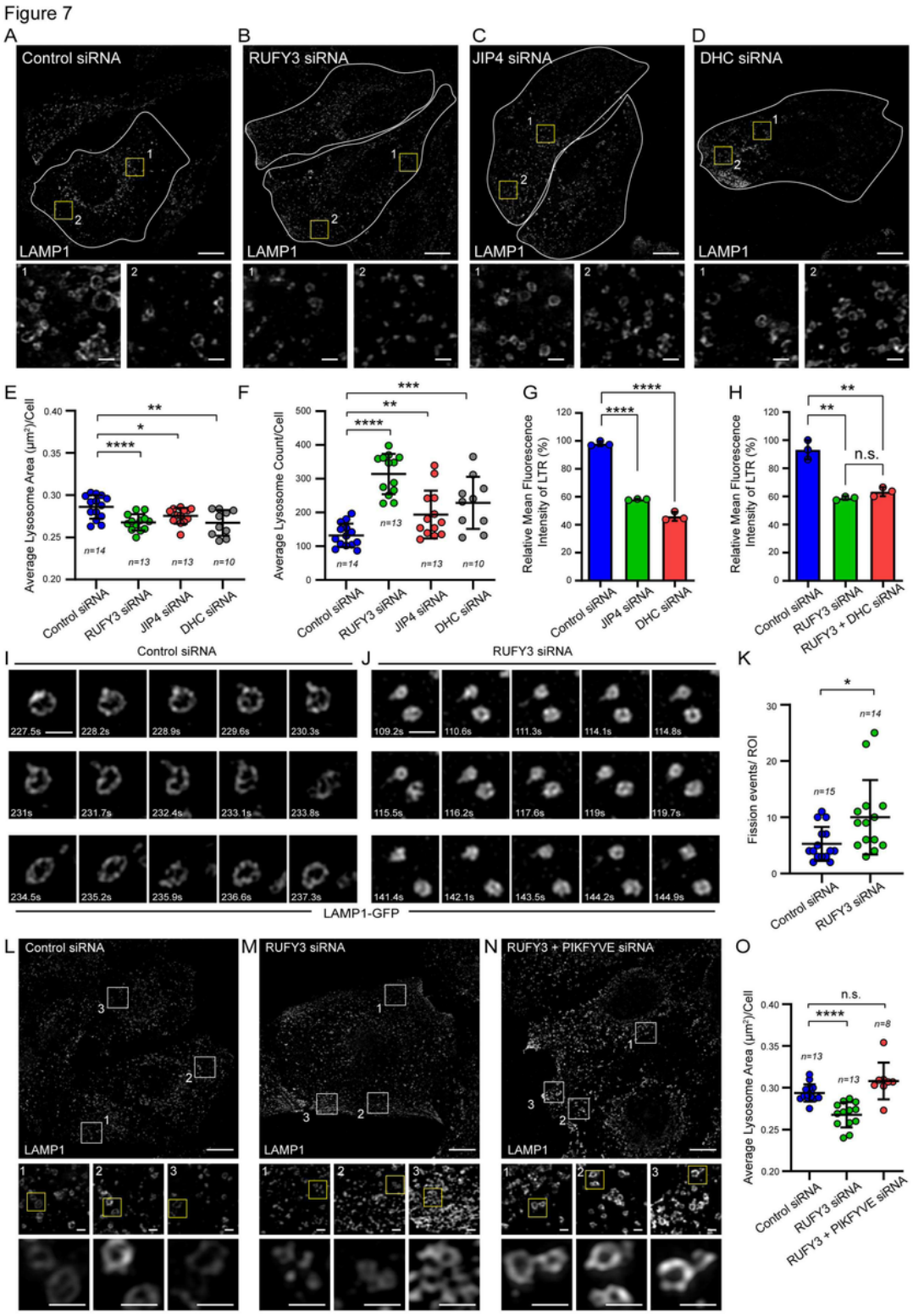

Figure 7

Depletion of retrograde transport machinery components reduces lysosome size and increases fission events. (A-D) Representative SIM images of HeLa cells transfected with indicated siRNAs and stained for lysosomes using anti-LAMP1 antibodies. Insets show a magnified view of boxed areas highlighting differences in lysosome size. Scale Bars: 10 μm (main); 1 μm (inset). (E-F) The average area (E) and count (F) of LAMP1-positive vesicles was measured in HeLa cells upon treatment with indicated siRNAs.

Values plotted are mean ± S.D. and the total number of cells analyzed is indicated on bottom of each data set (*p<0.05; **p<0.01; ***p<0.001; ****p<0.0001; Student's t-test). (G-H) Bar graph showing the percentage of relative MFI for Lysotracker Red DND-99 uptake (1 hr) in HeLa cells treated with indicated siRNAs. Values plotted are mean ± S.D. from three independent experiments. (I-J) Representative SIM micrographs from time-lapse imaging (see Supplementary Movies S4-5) showing LAMP1-GFP-positive vesicles undergoing tubulation or fission in control siRNA and RUFY3 siRNA treated HeLa cells. The movies were captured for 4 min on a super-resolution SIM microscope. Scale Bars: 1 μm. (K) Quantification of the number of fission events/region of interest (ROI) observed in HeLa cells treated with indicated siRNAs. Values plotted are mean ± S.D. from three independent videos, and the total number of ROI analyzed is indicated on top of each data set (*p<0.05; Student's t-test). (L-O) Representative SIM images of HeLa cells treated with indicated siRNAs and stained for lysosomes using an anti-LAMP1 antibody. In the insets, zoomed view of selected ROIs are shown, and quantification of the average area of lysosomes are plotted (O). Values plotted are mean ± S.D. from three independent experiments. The total number of ROI analysis is indicated on top of each data set (n.s., not significant; ****p<0.0001; Student's t-test). Scale Bars: 10 μm (main); 1 μm (inset).

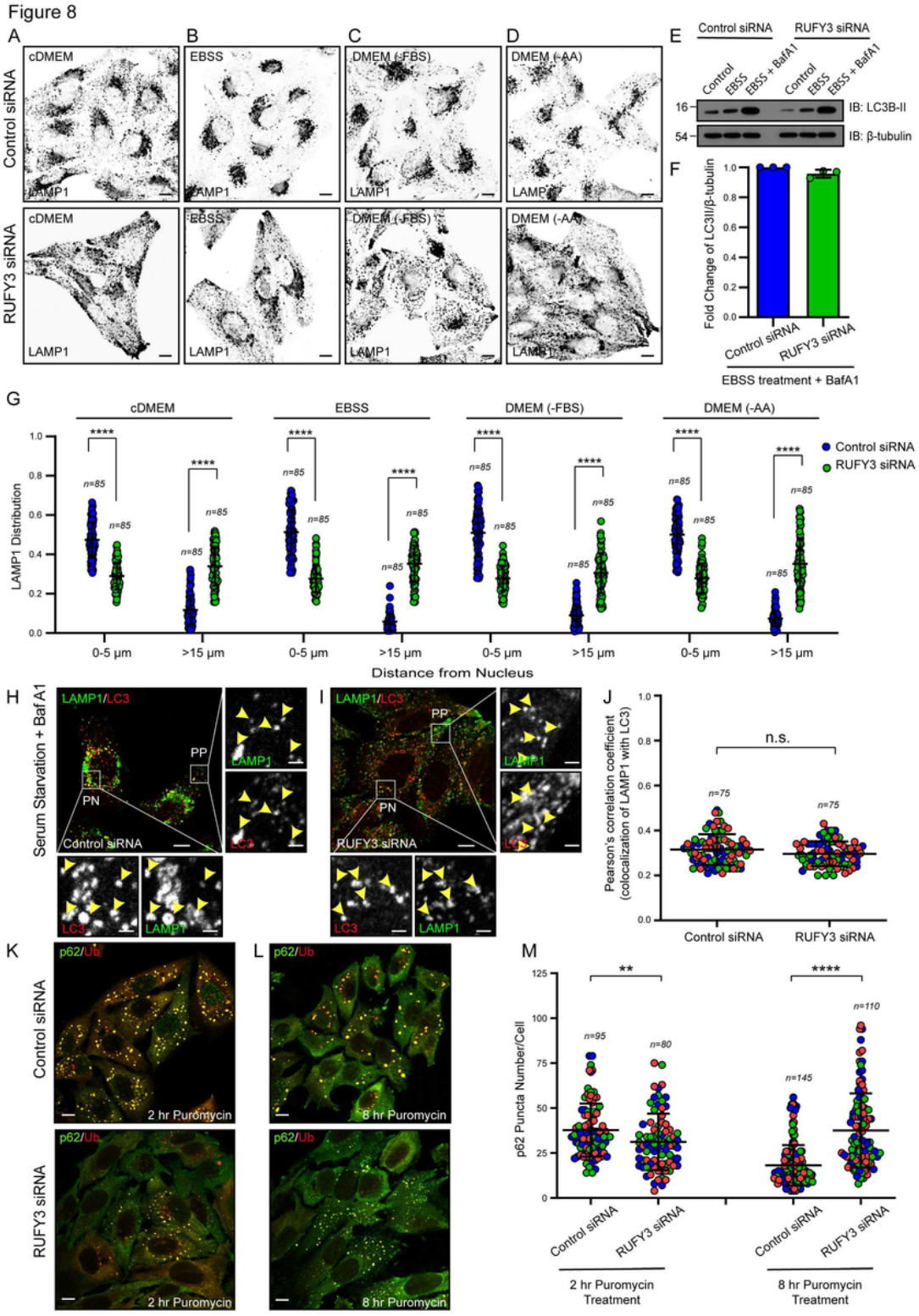

Figure 8

RUFY3 regulates nutrient-dependent lysosome repositioning but not autophagic cargo clearance. (A-D) Representative confocal images (shown as grayscale inverted) of HeLa cells treated with control siRNA or RUFY3 siRNA and incubated in indicated media for 4 hr. Post-treatment, cells were fixed and stained for lysosomes using an anti-LAMP1 antibody. Scale Bars: 10 μm. (E-F) HeLa cells transfected with control siRNA or RUFY3 siRNA were grown in complete media or subjected to 2 hr starvation using EBSS media

in the absence or presence of Bafilomycin A1 (BafA1). Lysates from these cell types were IB with the indicated antibodies. Protein densitometric analysis of LC3B-II levels normalized to β-tubulin is shown in (F). (G) The distribution of lysosomes based on the LAMP1 signal was performed in HeLa cells transfected with control siRNA or RUFY3 siRNA and subjected to incubation in indicated media for 4 hr. Values plotted are mean ± S.D. from three independent experiments, and the total number of cells analyzed is indicated on top of each data set (****p<0.0001; Student's t-test). (H-I) Representative confocal micrographs of control (H) and RUFY3-depleted (I) HeLa cells incubated in media lacking serum for 1 hr in the presence of BafA1. Post-treatment, cells were fixed and stained for LAMP1 and LC3. In the insets, selected peripheral (PP) and perinuclear (PN) regions of the cell are magnified to show colocalized pixels of LC3 with LAMP1 (denoted by yellow arrowheads). Scale Bars: 10 μm (main); 2 μm (inset). (J) Colocalization of LAMP1 with LC3 for the experiments performed in (H-I) was analyzed by measuring Pearson's correlation coefficient. Values plotted are mean ± S.D. from three independent experiments. Experiments are color-coded, and each dot represents the individual data points from each experiment. The total number of cells analyzed is indicated on top of each data set (n.s., not significant; Student's t-test). (K-L) Representative confocal micrographs of control and RUFY3-depleted HeLa cells incubated in media containing puromycin for 2 hr (K) or 8 hr (L). Post-treatment, cells were fixed and stained for p62 and Ubiquitin (Ub). Scale Bars: 10 μm. (M) The average number of p62 puncta/cell were quantified for the experiments shown in (K-L). Values plotted are mean ± S.D. from three independent experiments. Experiments are color-coded, and each dot represents the individual data points from each experiment. The total number of cells analyzed is indicated on top of each data set (**p<0.01; ****p<0.0001; Student's t-test).

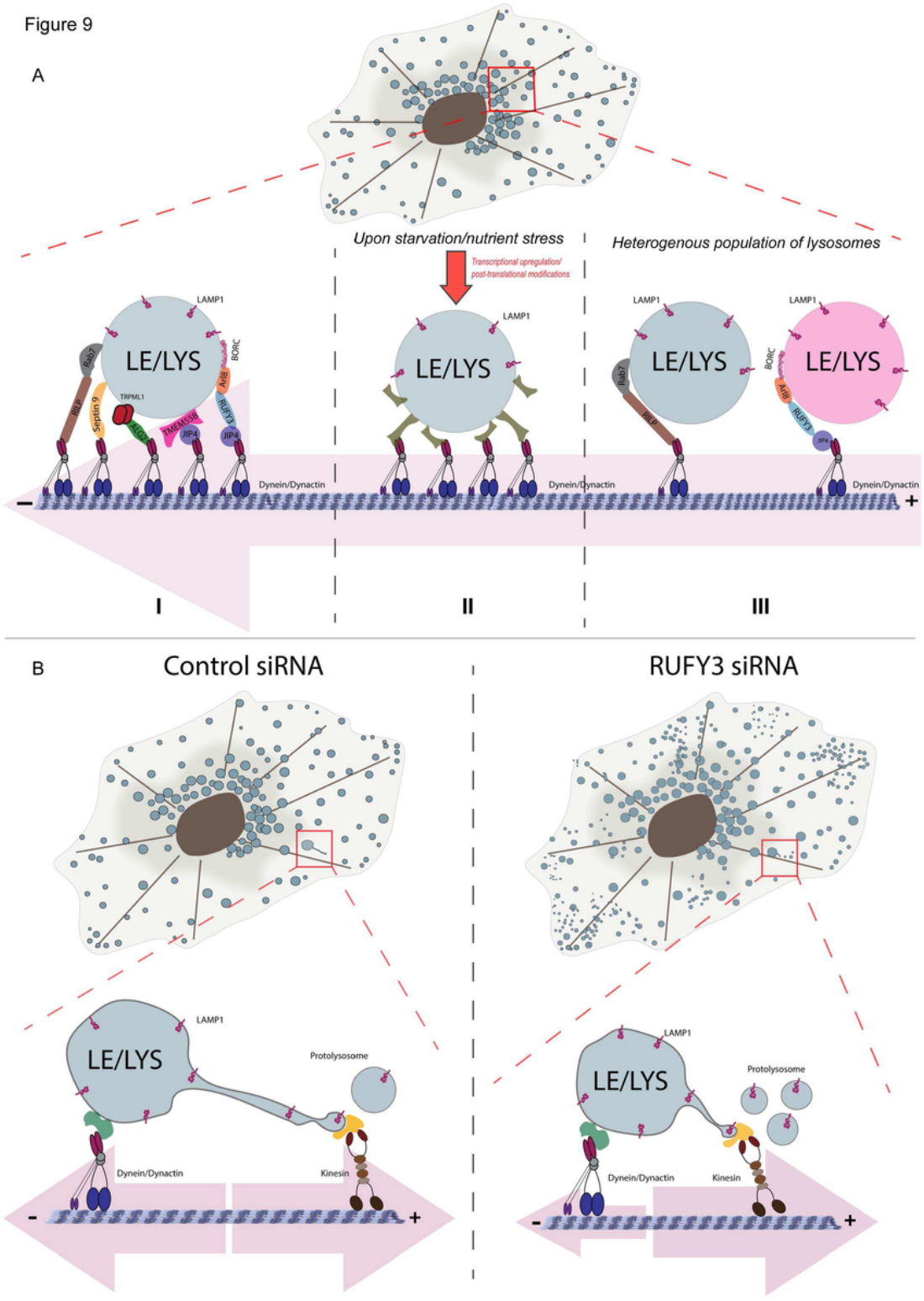

Figure 9

(A) Three distinct hypothetical scenarios to explain the significance of different lysosomal adaptors that engage the dynein-dynactin complex for retrograde transport. (I) Multiple adaptors may work in concert to recruit enough dynein motors to balance the opposite driving forces exerted by a single kinesin motor. (II) Different adaptors may be required under distinct physiological conditions. For instance, during nutrient starvation, expression and/or recruitment of a particular adaptor might increase onto lysosomes.

Increased spatial density of lysosomes and autophagosomes in the perinuclear region could enhance their fusion. (III) Different dynein adaptors are required for retrograde transport of distinct populations of lysosomes that may differ in their membrane composition. (B) Model illustrating the role of RUFY3 in maintaining the lysosome size. Left panel: Control cells showing predominantly a perinuclear distribution of lysosomes and few newly formed lysosomes. Both dynein and kinesin motors exert opposing forces on lysosomes to maintain a typical spatial distribution and probably lysosome size. Right panel: In RUFY3-silenced cells, dynein forces on lysosomes are reduced, leading to the peripheral distribution of lysosomes. As kinesin motor forces play a dominant role, more lysosome fission events are observed, resulting in smaller and numerous lysosomes.

Supplementary Files

This is a list of supplementary files associated with this preprint. Click to download.

- MovieS1.avi
- MovieS2.avi
- MovieS3.avi
- MovieS4.avi
- MovieS5.avi
- SupplementaryTableI.xlsx
- SupplementaryTableII.docx
- SupplementaryTableIII.docx
- SupplementaryFigureS1.pdf
- SupplementaryFigureS2.pdf
- SupplementaryFigureS3.pdf
- SupplementaryFigureS4.pdf
- SupplementaryFigureS5.pdf
- SupplementaryFigureS6.pdf
- SupplementaryFigureS7.pdf